

Phase curve pollution of exoplanet transmission spectra

GIUSEPPE MORELLO,^{1,2,3} TIZIANO ZINGALES,^{4,3} MARINE MARTIN-LAGARDE,¹ RENÉ GASTAUD,¹ AND
PIERRE-OLIVIER LAGAGE¹

¹*AIM, CEA, CNRS, Université Paris-Saclay, Université de Paris, F-91191 Gif-sur-Yvette, France*

²*Dept. of Physics & Astronomy, University College London, Gower Street, WC1E 6BT London, UK*

³*INAF-Osservatorio Astronomico di Palermo, Piazza del Parlamento 1, I-90134 Palermo, Italy*

⁴*Laboratoire d'astrophysique de Bordeaux, Univ. Bordeaux, CNRS, B18N, allée Geoffroy Saint-Hilaire, F-33615 Pessac, France*

Submitted to AJ

ABSTRACT

The occurrence of a planet transiting in front of its host star offers the opportunity to observe the planet's atmosphere filtering starlight. The fraction of occulted stellar flux is roughly proportional to the optically thick area of the planet, the extent of which depends on the opacity of the planet's gaseous envelope at the observed wavelengths. Chemical species, haze, and clouds are now routinely detected in exoplanet atmospheres through rather small features in transmission spectra, i.e., collections of planet-to-star area ratios across multiple spectral bins and/or photometric bands. Technological advances have led to a shrinking of the error bars down to a few tens of parts per million (ppm) per spectral point for the brightest targets. The upcoming James Webb Space Telescope (JWST) is anticipated to deliver transmission spectra with precision down to 10 ppm. The increasing precision of measurements requires a reassessment of the approximations hitherto adopted in astrophysical models, including transit light curve models. Recently, it has been shown that neglecting the planet's thermal emission can introduce significant biases in the transit depth measured with the JWST/Mid-InfraRed Instrument, integrated between 5 and 12 μm . In this paper, we take a step forward by analyzing the effects of the approximation on transmission spectra over the 0.6-12 μm wavelength range covered by various JWST instruments. We present open source software to predict the spectral bias, showing that, if not corrected, it may affect the inferred molecular abundances and thermal structure of some exoplanet atmospheres.

Keywords: Exoplanet atmospheres (487) – Transmission spectroscopy (2133) – Exoplanet systems (484) – Exoplanets (498) – Infrared observatories (791)

1. INTRODUCTION

The transit method has been the most successful for the detection and characterization of exoplanets to date. The CoRoT (Auvergne et al. 2009), Kepler (Borucki et al. 2010), and K2 (Howell et al. 2014) space missions have discovered nearly 3 000 transiting exoplanets. Ground-based surveys, such as HATNet (Bakos et al. 2004), HATSouth (Bakos et al. 2013), WASP (Pollacco et al. 2006), and TRAPPIST (Gillon et al. 2016), have

added hundreds of transiting exoplanets to the current census.

Transit photometry can reveal the size of the planet related to its host star and the orbital inclination based on the depth and duration of the drop in flux that occurs as the planet transits between the star and the observer for a fraction of its orbit. If combined with stellar spectra and radial velocity measurements, transit observations inform us about the mass, radius, mean density, and equilibrium temperature of exoplanets.

Transit spectroscopy provides insights into the atmospheres of exoplanets based on precise measurements of the transit depth at multiple wavelengths. Recently, the Wide Field Camera 3 (WFC3) on board the Hub-

ble Space Telescope (HST) delivered dozens of low-resolution transmission spectra in the 0.8-1.7 μm range (Iyer et al. 2016; Fu et al. 2017; Fisher & Heng 2018; Tsiaras et al. 2018). The HST/WFC3 spectra have revealed the presence of H_2O vapor in the atmosphere of several exoplanets down to super-Earth mass (Deming et al. 2013; Damiano et al. 2017; Benneke et al. 2019a; Tsiaras et al. 2019; Edwards et al. 2020) and hints of TiO (Evans et al. 2016), He (Mansfield et al. 2018; Spake et al. 2018), FeH (Skaf et al. 2020), H^- (Pluriel et al. 2020), and AIO (Chubb et al. 2020). Other HST and ground-based spectra in the UV and visible wavelengths have enabled detection of a long list of ions, atoms, haze, and clouds in some exoplanet atmospheres (Charbonneau et al. 2002; Vidal-Madjar et al. 2003, 2004; Fossati et al. 2010; Linsky et al. 2010; Parviainen et al. 2016; Chen et al. 2017, 2018). The Spitzer/InfraRed Array Camera (IRAC) broadband photometry at 3.6, 4.5, 5.8, and 8.0 μm has suggested the possible presence of carbon molecules (Beaulieu et al. 2011; Knutson et al. 2011; Morello et al. 2015). Combined spectra from different space- and/or ground-based instruments covering UV to infrared wavelengths have also been analyzed in the literature (Danielski et al. 2014; Sing et al. 2016; Barstow et al. 2017; Mancini et al. 2019; Pinhas et al. 2019; Luque et al. 2020).

Typical error bars in transit spectra can be a few tens to hundreds of parts per million (ppm). The upcoming James Webb Space Telescope (JWST) will provide infrared spectra with unprecedented precision down to ~ 10 ppm for some targets (Beichman et al. 2014). The Ariel mission aims to perform similarly high-precision transit spectroscopy over a statistical sample of ~ 1000 exoplanet atmospheres (Tinetti et al. 2018). In parallel with the improvements of instruments and observational techniques, it is necessary to develop more detailed models to adequately represent astrophysical phenomena, such as stellar limb-darkening, and magnetic activity (Micela 2015; Scandariato & Micela 2015; Morello et al. 2017; Morello 2018; Sarkar et al. 2018).

Here we discuss the impact of the “dark planet” approximation in transit spectroscopy. As the planet is orders of magnitude fainter than the host star, its flux contribution is usually neglected when modeling the transit light curves (Mandel & Agol 2002). Kipping & Tinetti (2010) pointed out that the measured transit depth tends to be underestimated due to the planetary flux acting as a self-blend. They evaluated that the bias in transit depth could be down to -100 ppm for some hot Jupiters observed in the thermal infrared. Martin-Lagarde et al. (2020) showed that the transit depth can also be overestimated due to the variation of the emer-

gent planetary flux with the orbital phase, the so-called “phase-blend” effect. They predicted the total bias in transit depth for a sample of exoplanets observed with the JWST/Mid-InfraRed Instrument (MIRI) to be between -100 and +550 ppm, depending on the system parameters and exoplanet atmospheric properties. They also noted that, unlike the self-blend, the phase-blend effect is degenerate with instrumental systematics that can be detrended from the data.

In this paper, we explore how self- and phase-blend biases can alter the transmission spectra of exoplanet atmospheres and consequently affect scientific inferences.

Structure of the paper—Section 2 describes the newly released `ExoTETHyS.BOATS` subpackage, with particular emphasis on the procedure to compute the self- and phase-blend biases. Section 3 discusses some examples of spectral biases. Section 4 presents a study of simulated spectra obtained with JWST spectrographs. Section 5 discusses the potential impact of self- and phase-blend bias in future observations with JWST, focusing on the targets that are already scheduled. Section 6 summarizes the conclusions of our study.

2. THE EXOTETHYS.BOATS SUBPACKAGE

We present here a new tool designed to estimate the Bias in the Occultation Analysis of Transiting Systems (BOATS). The BOATS subpackage¹ is part of `ExoTETHyS`, an open-source software that collects a set of tools for modeling exoplanetary transits and their host stars (Morello et al. 2020b,a). All of the code within `ExoTETHyS` is written in python 3.

The BOATS subpackage contains several functions designed to obtain the spectra of astrophysical objects, to perform specific operations on these spectra (e.g., conversions, integration over instrumental passbands, time intervals and/or areas, and composition of spectra), and to compute some properties of transiting exoplanets (e.g., transit duration, atmospheric temperatures, albedo, and circulation efficiency).

In this paper, we describe how to use the BOATS subpackage to obtain estimates of the potential self- and phase-blend biases in observations of exoplanetary transits.

2.1. Input and Output

The procedure requires a configuration file to perform the full set of predetermined calculations for a given exoplanet transit or eclipse. The user can choose between

¹ <https://github.com/ucl-exoplanets/ExoTETHyS/blob/master/exotethys/boats.py>

several model grids with precalculated stellar spectra, use a blackbody spectrum, or read the stellar spectrum from a file. The choice for exoplanets is between blackbody and user file spectra to model their dayside and nightside emission. In the case of spectra read from user files, it is necessary to specify whether these spectra are to be rescaled by the distance and radius of the source to obtain the observed flux. The input planetary spectra can be given in absolute units or normalized with respect to the stellar spectrum, such as those typically obtained by running forward models of the secondary eclipses with NEMESIS (Irwin et al. 2008), CHIMERA (Line et al. 2013), and Tau-REx II (Waldmann et al. 2015) and III (Al-Refaie et al. 2019).

The user must request one or more instrumental passbands. Some passbands are built into the ExoTETHyS package through text files that report the photon-to-electron conversion efficiencies (PCEs) at given wavelengths. User files with the same format can also be accepted. Optionally, the passbands can be split into multiple wavelength bins, as is usual in exoplanet transit spectroscopy.

Other mandatory input information includes the area of the telescope (\mathcal{A}_{tel}), the duration of the simulated observation (Δt_{obs}), and a set of parameters of the star-planet system. The distance of the system from the Earth (d) and the telescope area can be used to rescale the template spectra in order to match the photon count rates received by the detector. We anticipate here that rescaling by d and \mathcal{A}_{tel} does not affect the transit depth biases, only the nominal error bars.

The input stellar parameters are the effective temperature ($T_{*,\text{eff}}$), surface gravity ($\log g_*$), metallicity ($[\text{M}/\text{H}]_*$), and radius (R_*). The stellar models in the grids are identified by $T_{*,\text{eff}}$, $\log g_*$, and $[\text{M}/\text{H}]_*$. The default values of $\log g_* = 4.5$ and $[\text{M}/\text{H}]_* = 0.0$ are implemented if these parameters are missing in the configuration file. The blackbody spectrum is defined by $T_{*,\text{eff}}$ alone. If the stellar spectrum is obtained from a user file, none of these three parameters is necessary, unless $T_{*,\text{eff}}$ is required to calculate the planetary spectra. Here R_* is always mandatory.

The orbital period (P), semimajor axis (a), inclination (i), and planet radius (R_p) are needed to determine the geometry of the transit. The planet’s emission is modeled through two spectra from the dayside and nightside hemispheres, either blackbody or user-supplied spectra. The blackbody spectra can be defined by directly setting the dayside and nightside temperatures (T_{day} , T_{night}), or by means of the bond albedo (A_b) and circulation efficiency (ε).

Each physical parameter, except for temperatures and dimensionless parameters, is defined through two keywords in the configuration file to give its numerical value and the corresponding unit. The `astropy.units` package is used to interpret the input units and to handle operations between physical quantities. Additionally, R_p and a can be expressed in units of R_* , and Δt_{obs} can be relative to the total transit duration (T_{1-4}).

The output is a text or pickle file containing estimates of transit depth biases and error bars for the requested exoplanet systems and passbands.

2.2. Flux conversions

The stellar model atmosphere grids consist of one file for each triple of stellar parameters ($T_{*,\text{eff}}$, $\log g_*$, $[\text{M}/\text{H}]_*$), containing the emergent spectrum at the star surface in units of $\text{erg cm}^{-2} \text{s}^{-1} \text{\AA}^{-1}$. The same files also include spatially resolved intensities, which are used by other subpackages to model limb-darkening. The BOATS algorithm first calculates the spectral photon rates collected by the telescope in units of $\text{photons s}^{-1} \text{\AA}^{-1}$. In order to do so, the stellar and planetary spectra are multiplied by $(R/d)^2 \mathcal{A}_{\text{tel}}$, where R is the object’s radius. The geometric dilution factor $(R/d)^2$ can be set to 1 for a user file spectrum by selecting the no-rescale flux option.

The next step is to compute the electron rates of detectors. This is done by multiplying the photon rates by the PCE and integrating on the passband or wavelength bin. In the following subsections, we will refer to fluxes (symbol F) as equivalent to electron rates in $\text{e}^- \text{s}^{-1}$, calculated as described here.

2.3. Exoplanet phase curve model

The BOATS calculations rely on a toy model to describe the phase curve modulations. The observed planet flux is

$$F_p = \psi F_{\text{day}} + (1 - \psi) F_{\text{night}}, \quad (1)$$

where F_{day} and F_{night} denote the emergent flux from the two hemispheres of the planet, and ψ is the fraction of the area of the planet’s projection showing the dayside. Other assumptions (valid for ExoTETHyS version 2.0.0) are that the planet lies on a circular, edge-on orbit, in synchronous rotation with zero obliquity, and the dayside is centered on the substellar point. Under these hypotheses, we have

$$\psi = \frac{1 - \cos \varphi}{2}, \quad (2)$$

where

$$\varphi = \frac{2\pi}{P} t \quad (3)$$

is the orbital phase angle, and t is the time from mid-transit. This toy model is identical to that adopted by the `ExoNoodle` software (Martin-Lagarde et al. 2020, 2021), but with one less degree of freedom relative to the centering of the dayside hemisphere with respect to the substellar point. It relies on the simplest hypotheses that enable order-of-magnitude estimates of the possible self- and phase-blend effects, solely based on the easiest-to-measure system parameters.

If Blackbody is the selected grid of planetary models, the two temperatures, T_{day} and T_{night} , can also be determined from the atmospheric parameters A_b and ε (Cowan & Agol 2011),

$$\begin{cases} T_{\text{day}} = T_{\text{irr}} (1 - A_b)^{\frac{1}{4}} \left(\frac{2}{3} - \frac{5}{12} \varepsilon \right)^{\frac{1}{4}} \\ T_{\text{night}} = T_{\text{irr}} (1 - A_b)^{\frac{1}{4}} \left(\frac{\varepsilon}{4} \right)^{\frac{1}{4}} \end{cases}, \quad (4)$$

where the irradiation temperature is

$$T_{\text{irr}} = T_{*,\text{eff}} \sqrt{\frac{R_*}{a}}. \quad (5)$$

In general, the dayside flux is the sum of planetary intrinsic emission and reflected starlight,

$$F_{\text{day}} = F_{\text{day}}^{\text{emission}} + F_{\text{day}}^{\text{reflection}}, \quad (6)$$

where $F_{\text{day}}^{\text{emission}}$ is calculated from the corresponding blackbody or user spectrum, and

$$F_{\text{day}}^{\text{reflection}} = A_b \left(\frac{R_p}{2a} \right)^2 F_*, \quad (7)$$

with F_* being the stellar flux. The nightside flux consists of a pure planetary emission component.

2.4. Phase-averaged fluxes

The next important step is to calculate the mean flux of the planet during and out of the transit. Given the symmetry of the phase curve model described in section 2.3, and assuming that the observation interval is centered on the transit, it is sufficient to consider the half observation after the mid-transit point. The transit event is delimited by the external contact points; the corresponding duration is (Seager & Mallén-Ornelas 2003)

$$T_{1-4} = \frac{P}{\pi} \arcsin \left(\frac{\sqrt{\left(1 + \frac{R_p}{R_*}\right)^2 - \left(\frac{a}{R_*} \cos i\right)^2}}{\frac{a}{R_*} \sin i} \right). \quad (8)$$

The phase angles corresponding to the end of the transit and of the observation are

$$\frac{\Phi_{1-4}}{2} = \frac{\pi}{P} T_{1-4}, \text{ and } \frac{\Delta\varphi_{\text{obs}}}{2} = \frac{\pi}{P} \Delta t_{\text{obs}}. \quad (9)$$

By using Equations 1-3, the phase-averaged fluxes are

$$F_p^{\text{in}} = \frac{2}{\Phi_{1-4}} \int_0^{\frac{\Phi_{1-4}}{2}} F_p d\phi = F_{\text{day}} \bar{\psi}^{\text{in}} + F_{\text{night}} (1 - \bar{\psi}^{\text{in}}), \text{ and} \quad (10)$$

$$F_p^{\text{out}} = \frac{2}{\Delta\varphi_{\text{obs}} - \Phi_{1-4}} \int_{\frac{\Phi_{1-4}}{2}}^{\frac{\Delta\varphi_{\text{obs}}}{2}} F_p d\phi = F_{\text{day}} \bar{\psi}^{\text{out}} + F_{\text{night}} (1 - \bar{\psi}^{\text{out}}), \quad (11)$$

with

$$\bar{\psi}^{\text{in}} = \frac{1}{2} \left(1 - \frac{\sin\left(\frac{\Phi_{1-4}}{2}\right)}{\frac{\Phi_{1-4}}{2}} \right), \text{ and} \quad (12)$$

$$\bar{\psi}^{\text{out}} = \frac{1}{2} \left(1 - \frac{\sin\left(\frac{\Delta\varphi_{\text{obs}}}{2}\right) - \sin\left(\frac{\Phi_{1-4}}{2}\right)}{\frac{\Delta\varphi_{\text{obs}}}{2} - \frac{\Phi_{1-4}}{2}} \right). \quad (13)$$

2.5. Transit depth bias and error bars

The transit depth is defined as the planet-to-star projected area ratio,

$$p^2 = \left(\frac{R_p}{R_*} \right)^2. \quad (14)$$

Finally, the self- and phase-blend effects are calculated as (Martin-Lagarde et al. 2020, see their Figure 2)

$$(\Delta p^2)_{\text{self-blend}} = -\frac{F_p^{\text{out}}}{F_* + F_p^{\text{out}}} p^2, \text{ and} \quad (15)$$

$$(\Delta p^2)_{\text{phase-blend}} = \frac{F_p^{\text{out}} - F_p^{\text{in}}}{F_* + F_p^{\text{out}}}, \quad (16)$$

and the total bias in transit depth is

$$\Delta p^2 = (\Delta p^2)_{\text{self-blend}} + (\Delta p^2)_{\text{phase-blend}}. \quad (17)$$

In the photon noise limit, the minimum error bar depends on the number of electrons produced in and out of the transit. Ignoring the ingress, egress, and limb-darkening effects, these numbers are

$$N^{\text{in}} = (F_*(1 - p^2) + F_p^{\text{in}}) T_{1-4}, \text{ and} \quad (18)$$

$$N^{\text{out}} = (F_* + F_p^{\text{out}}) (\Delta t_{\text{obs}} - T_{1-4}). \quad (19)$$

The nominal error bar is

$$\sigma_{p^2} = (1 - p^2) \sqrt{\frac{1}{N^{\text{in}}} + \frac{1}{N^{\text{out}}}}. \quad (20)$$

We note that the actual error bar obtained by fitting the light curve data can be larger because of the parameter correlations and additional noise components.

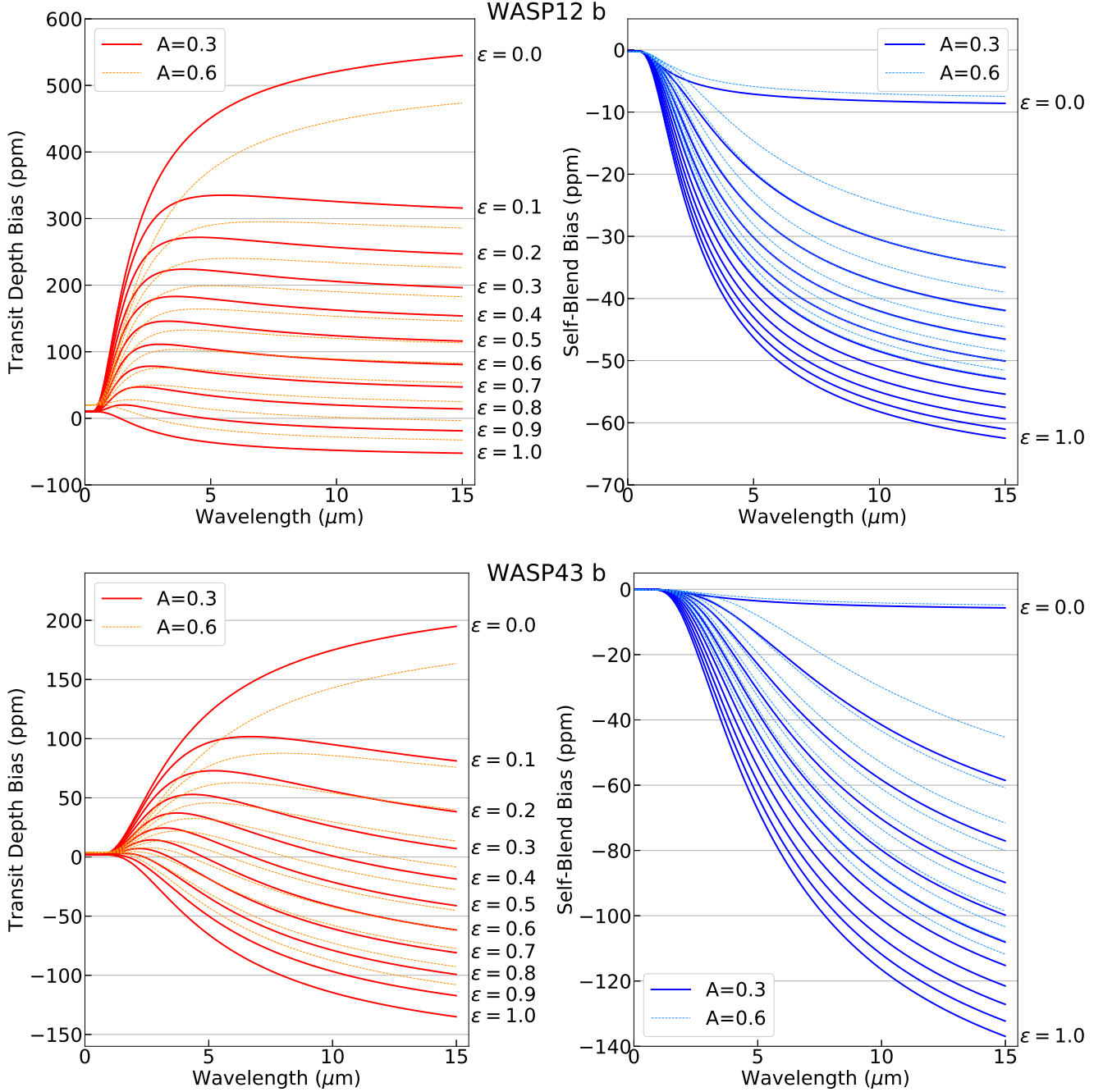


Figure 1. Top left panel: total transit depth bias (in ppm) vs. wavelength for WASP 12 b. We assume pure blackbody emission from the exoplanet dayside and nightside hemispheres, different values of the atmospheric circulation efficiency ($0 \leq \epsilon \leq 1$, step of 0.1), and bond albedo ($A_b = 0.3, 0.6$). Top right panel: Analogous plot for the self-blend bias only. Bottom panels: Analogous plots for WASP 43 b. The self- and phase-blend bias increase in absolute value with wavelength as the star–planet contrast decreases. The self-blend (phase-blend) bias is always negative (positive), and it is larger with a higher (lower) circulation efficiency. The bond albedo acts as a scaling factor. The total bias is the sum of the two terms. The phase-blend alone is not shown, as it cannot be the only bias term.

3. SPECTROSCOPIC TRENDS

It is evident from the Equations 15 and 16 that the transit depth bias due to the dark planet approximation is wavelength-dependent, being a function of stellar and

planetary fluxes. Consequently, it can alter the measurements of the transmission spectra of the exoplanet atmospheres.

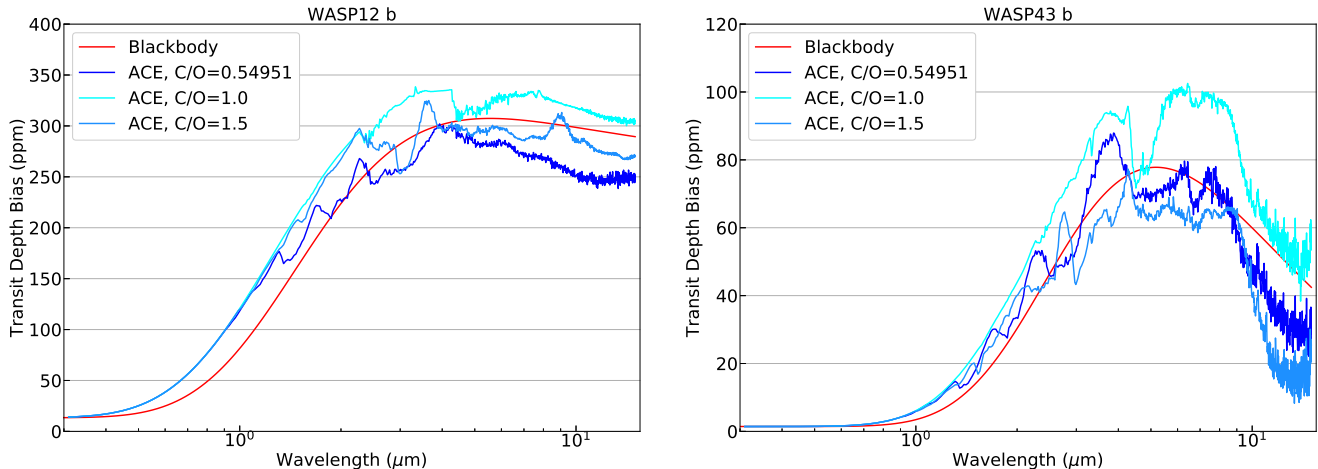


Figure 2. Left panel: total transit depth bias (in ppm) vs. wavelength for WASP 12 b, assuming a pure blackbody (red), ACE with solar C/O ratio (blue), and C/O=1 (cyan) and 1.5 (dodger blue) emission spectra from the dayside and nightside hemispheres. The temperatures are fixed to the most likely values reported in Table 3. Right panel: Analogous plot for WASP 43 b.

Instrument	Range λ (μm)	Bin $\Delta\lambda$ (μm)
NIRISS SOSS	0.60–2.80	0.02–0.1 ^a
NIRSpec G235H	1.66–3.17	0.03
NIRSpec G395H	2.87–5.27	0.04
MIRI LRS	5.0–12.0	0.1–0.2 ^b

^aNIRISS SOSS: $\Delta\lambda = 0.02$ if $0.92 < \lambda < 1.98$, $\Delta\lambda = 0.03$ if $0.80 < \lambda < 0.92$ or $1.98 < \lambda < 2.34$, $\Delta\lambda = 0.04$ if $2.34 < \lambda < 2.50$, $\Delta\lambda = 0.05$ if $0.70 < \lambda < 0.80$ or $2.50 < \lambda < 2.80$, and $\Delta\lambda = 0.10$ if $0.60 < \lambda < 0.70$.

^bMIRI LRS: $\Delta\lambda = 0.1$ if $5.0 < \lambda < 9.0$, and $\Delta\lambda = 0.2$ if $9.0 < \lambda < 12.0$.

Table 1. Nominal wavelength ranges and choice of bin sizes for the selected JWST observing modes.

Figure 1 shows the spectroscopic biases obtained for two systems with different values of bond albedo and circulation efficiency of the exoplanet atmospheres, assuming pure blackbody emissions. In all cases, the bias appears to be very small in the UV and visible, and it tends to be larger at wavelengths $\gtrsim 1 \mu\text{m}$. The spectrum bias has a smaller amplitude with higher albedo due to the lower temperatures of the exoplanet atmosphere, but the overall trend is weakly dependent on the albedo.

Most configurations for WASP 12 b have a positive spectrum bias; i.e., the phase-blend bias is larger than the self-blend bias. In this case, the largest bias occurs with the minimum circulation efficiency. The dominant effect for WASP 43 b depends on the circulation efficiency. If $\epsilon \sim 0.5$, the spectrum bias has both positive

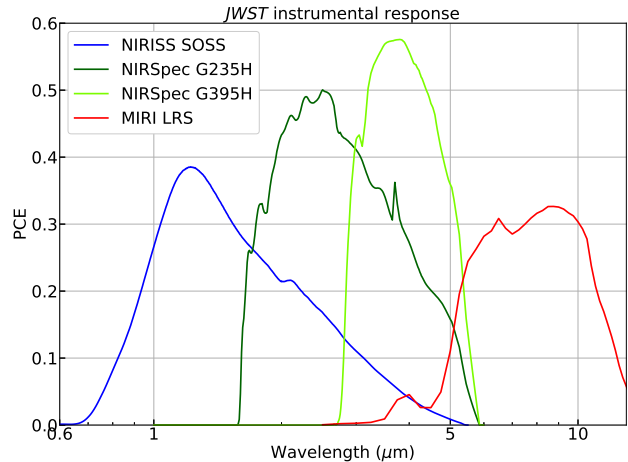


Figure 3. The PCEs for the JWST NIRISS SOSS (blue), NIRSpec G235H (dark green), NIRSpec G395H (light green), and MIRI LRS (red) instrumental setups adopted in our simulations.

and negative values. In general, the phase-blend component of the bias can be largely removed with conventional detrending practices, albeit by mixing astrophysical signals with instrumental systematic effects (Martin-Lagarde et al. 2020). It is worth pointing out that the correction of the phase-blend effect must be wavelength-dependent, as a white light curve correction would not attenuate the spectral bias. The remaining self-blend bias increases monotonically in absolute value with the atmospheric circulation efficiency. The self-blend effect can only be corrected with full phase curve observations or by relying on theoretical models.

Figure 2 compares the spectroscopic biases obtained with blackbody and equilibrium chemistry spectra for

Planet	R_p (R_J)	a (au)	i (deg)	P (days)	R_* (R_\odot)	$T_{*,\text{eff}}$ (K)	d (pc) ^a	References
WASP 12 b	1.9	0.02339	83.37	1.0914203	1.657	6360	432.589	Collins et al. (2017)
WASP 43 b	0.93	0.0142	82.6	0.813475	0.6	4400	86.9633	Hellier et al. (2011)
WASP 121 b	1.865	0.02544	87.6	1.2749255	1.458	6460	272.013	Delrez et al. (2016)
WASP 18 b	1.158	0.02034	85.0	0.94145181	1.222	6400	123.925	Southworth (2010)
WASP 79 b	1.53	0.0519	86.1	3.662392	1.51	6600	248.447	Brown et al. (2017)
WASP 80 b	0.999	0.0344	89.02	3.06785234	0.586	4143	49.8591	Triaud et al. (2015)
WASP 17 b	1.991	0.0515	86.83	3.7354380	1.572	6650	410.408	Anderson et al. (2011)
WASP 39 b	1.27	0.0486	87.83	4.055259	0.895	5400	215.295	Faedi et al. (2011)
WASP 69 b	1.057	0.04527	86.71	3.8681382	0.813	4715	50.0323	Bonomo et al. (2017) Wallack et al. (2019)
HD 189733 b	1.138	0.03099	85.58	2.218573	0.756	5040	19.7752	Torres et al. (2008)
HD 209458 b	1.359	0.04707	86.71	3.524746	1.155	6065	48.3688	Torres et al. (2008)
HD 149026 b	0.654	0.04313	90.0	2.87588874	1.368	6160	76.0306	Torres et al. (2008)
HAT-P-1 b	1.242	0.0553	86.11	4.46543	1.135	5975	159.706	Torres et al. (2008)
HAT-P-26 b	0.565	0.04357	88.09	4.2345023	0.788	5011	142.408	Wakeford et al. (2017) Wallack et al. (2019)
GJ 436 b	0.3767	0.02872	86.36	2.6438983	0.464	3350	9.7559	Torres et al. (2008)
GJ 3470 b	0.34615	0.031	88.88	3.3366487	0.48	3652	29.4463	Biddle et al. (2014) Benneke et al. (2019b)
WASP 77A b	1.21	0.024	89.4	1.3600309	0.955	5500	105.465	Maxted et al. (2013)
WASP 52 b	1.27	0.0272	85.35	1.7497798	0.79	5000	175.691	Hébrard et al. (2013)
WASP 127 b	1.41	0.0522	88.1	4.178062	1.33	5750	160.233	Lam et al. (2017)
WASP 107 b	0.94	0.055	89.7	5.721490	0.66	4430	64.8614	Anderson et al. (2017)
TOI 193 b	0.45	0.0169	75.4	0.7921	0.99	5222	80.6231	Pearson (2019)
GJ 1214 b	0.254	0.01411	88.17	1.58040456	0.216	3026	14.6487	Harp�s�e et al. (2013)
GJ 357 b	1.217	0.035	89.12	3.93072	0.337	3505	9.4444	Luque et al. (2019)
GJ 1132 b	1.16	0.0154	88.64	1.628930	0.207	3270	12.6176	Berta-Thompson et al. (2015)
L98-59 c	0.12023	0.0324	89.3	3.690621	0.312	3367	10.6226	Kostov et al. (2019)
L98-59 d	0.14027	0.052	88.5	7.45086	0.312	3367	10.6226	Kostov et al. (2019)
LP 791-18 b	0.09992	0.00969	87.3	0.9480050	0.171	2960	26.5128	Crossfield et al. (2019)
Trappist-1 b	0.101914	0.011534	89.28	1.51088432	0.1234	2520	12.4299	Ducrot et al. (2020)
Trappist-1 d	0.072085	0.02226	89.65	4.04978035	0.1234	2520	12.4299	Ducrot et al. (2020)
Trappist-1 e	0.084263	0.02924	89.663	6.09956479	0.1234	2520	12.4299	Ducrot et al. (2020)
Trappist-1 f	0.096128	0.038774	89.666	9.20659399	0.1234	2520	12.4299	Ducrot et al. (2020)

^aThe distances of the systems have been taken from the Gaia Data Release 2 catalog (Gaia Collaboration et al. 2018).

Table 2. Adopted system parameters.

the exoplanet dayside and nightside. These latter spectra can introduce some molecular features in addition to the smooth trend obtained with blackbody spectra.

4. BIASED RETRIEVAL ANALYSES

In this section, we describe the simulations aimed at characterizing the scientific impact of potential bias in the transmission spectra of exoplanet atmospheres observed with JWST. The essential steps of this study are:

1. creating the reference transmission spectra,

2. computing the spectroscopic bias and the corresponding biased spectra under different hypotheses,

3. performing atmospheric retrievals on the biased transmission spectra, and

4. comparing the retrieved atmospheric properties with those of the reference transmission spectra.

Planet	Obs. Type ^a	Most likely configurations			Extreme configurations	
		$T_{\text{day}}/T_{\text{night}}$ (K)	A_b, ε	References	$T_{\text{day}} (T_{\text{night}} = 0 \text{ K})$	$T_{\text{day}} = T_{\text{night}} (K)$
					$A_b = 0, \varepsilon = 0$	$A_b = 0, \varepsilon = 1$
WASP 12 b	phase curve	2850/1350	0.40, 0.12	Bell et al. (2019)	3299	2581
WASP 43 b	phase curve	1600/850	0.23, 0.19	Morello et al. (2019)	1762	1379
WASP 121 b	phase curve	2950/1170	0.044, 0.064	Daylan et al. (2021)	3014	2358
WASP 18 b	phase curve	2890/480	0.20, 0.002	Arcangeli et al. (2019)	3057	2392
WASP 79 b	eclipse	1950/1510	0.0, 0.60	Garhart et al. (2020)	2194	1717
WASP 80 b	eclipse	890/770	0.0, 0.77	Triaud et al. (2015)	1054	825
WASP 17 b	eclipse	1730/1730	0.091, 1.0	Anderson et al. (2011)	2264	1772
WASP 39 b	eclipse	1130/1110	0.0, 0.97	Kammer et al. (2015)	1428	1117
WASP 69 b	eclipse	940/940	0.094, 1.0	Wallack et al. (2019)	1231	964
HD 189733 b	phase curve	1250/990	0.27, 0.63	Knutson et al. (2009, 2012)	1534	1200
HD 209458 b	phase curve	1500/970	0.44, 0.36	Zellem et al. (2014)	1851	1449
HD 149026 b	phase curve	1800/1030	0.41, 0.24	Zhang et al. (2018)	2138	1673
HAT-P-1 b	eclipse	1500/1120	0.0, 0.55	Todorov et al. (2010)	1668	1305
HAT-P-26 b	eclipse	700/700	0.78, 1.0	Wallack et al. (2019)	1313	1028
GJ 436 b	eclipse	790/480	0.0, 0.28	Stevenson et al. (2010)	830	649
GJ 3470 b	eclipse	510/510	0.71, 1.0	Benneke et al. (2019b)	886	693
WASP 77A b	none	–	–	–	2138	1673
WASP 52 b	none	–	–	–	1660	1299
WASP 127 b	none	–	–	–	1788	1400
WASP 107 b	none	–	–	–	946	740
TOI 193 b	none	–	–	–	2463	1927
GJ 1214 b	none	–	–	–	730	571
GJ 357 b	none	–	–	–	670	524
GJ 1132 b	none	–	–	–	739	578
L98-59 c	none	–	–	–	644	504
L98-59 d	none	–	–	–	508	398
LP 791-18 d	none	–	–	–	766	600
Trappist-1 b	none	–	–	–	508	397
Trappist-1 d	none	–	–	–	366	286
Trappist-1 e	none	–	–	–	319	250
Trappist-1 f	none	–	–	–	277	217

^aType of observations used to estimate T_{day} and T_{night} (most likely configurations). Whereas multiple observations were available, we took the arithmetic average of the brightness temperatures reported in the reference paper. The eclipse observations provide T_{day} only; the corresponding T_{night} was calculated by assuming the maximum circulation efficiency compatible with the eclipse data.

Table 3. Adopted T_{day} , T_{night} , A_b , and ε based on the available observations, and/or for the extreme cases that maximise the phase- and self-blend, respectively.

We selected two targets among those that showed potentially significant bias in infrared transit photometry according to [Martin-Lagarde et al. \(2020\)](#).

- WASP 12 b has the largest predicted bias (positive) in their sample. It is the subject of several theoretical studies and past observations ([Cowan](#)

[et al. 2012](#); [Stevenson et al. 2014b,a](#); [Kreidberg et al. 2015](#); [Bell et al. 2019](#)).

- WASP 43 b can have one of the largest positive or negative biases, depending on its atmospheric circulation efficiency. It is the subject of many theoretical studies and past and future observations ([Stevenson et al. 2014c, 2017](#); [Keating &](#)

Cowan 2017; Bean et al. 2018; Mendonça et al. 2018; Morello et al. 2019; May & Stevenson 2020; Venot et al. 2020).

These planets represent hot Jupiters with ultrashort orbital periods around different types of host stars.

4.1. Reference transmission spectra

We took the transmission spectra observed with HST/WFC3 as starting points. In particular, we reanalyzed the low-resolution spectra at 1.1-1.7 μm reported by Tsiaras et al. (2018) using the novel Tau-REx III retrieval algorithm (Al-Refaie et al. 2019). As the narrow wavelength range limits the ability to detect molecules other than H_2O , we adopted atmospheric chemical equilibrium (ACE) models (Agúndez et al. 2012; Venot et al. 2012) instead of the most popular free chemistry to include more absorbing species. The molecular absorption cross sections were computed by the ExoMol group (Chubb et al. 2021). We also included collisionally induced absorption (CIA) by $\text{H}_2\text{-H}_2$ and $\text{H}_2\text{-He}$ (Gordon et al. 2017) and Mie scattering (Lee et al. 2013). We assumed an isothermal temperature profile.

The free parameters in our retrievals were the planet radius at 10 bar, the atmospheric temperature, Mie scattering cloud particle size, mixing ratio, and composition. The carbon-to-oxygen (C/O) ratio and metallicity were fixed to solar values. The best-fit solutions obtained with these settings have the same Bayesian evidence as those reported by Tsiaras et al. (2018) to within $\Delta \log E \leq 2$, despite using only five free parameters instead of 12 and 10 for WASP 12 b and WASP 43 b, respectively.

We calculated forward model spectra that extend the best-fit solutions over a broader wavelength range, then bin-averaged. In this way, we obtained the transmission spectra associated with three JWST instruments using the same observing modes planned for the Transiting Exoplanet Community ERS program (Bean et al. 2018):

- the Near-InfraRed Imager and Slitless Spectrograph (NIRISS) with the Single-Object Slitless Spectroscopy (SOSS) mode,
- the Near-InfraRed Spectrograph (NIRSpec) with the G235H and G395H gratings, and
- the MIRI with the Low-Resolution Spectroscopy (LRS) slitless mode.

Table 1 reports the nominal wavelength ranges for the three instruments and the size of the spectroscopic bins. Figure 3 shows the corresponding PCEs. The

PCE for each observing setup is the combined throughput from the telescope, instrument optics, detector efficiency, quantum efficiency, and filter throughput (if applicable). We adopted the reference data files from the Pandeia Exposure Time Calculator (Pontoppidan et al. 2016), and precalculated response functions for the MIRI LRS slitless (Kendrew et al. 2015) and NIRISS SOSS (Maszkiewicz 2017). The resulting PCEs are among the passbands available within the ExoTETHyS package.

Additionally, we considered another set of reference transmission spectra with identical parameters, except for C/O=1.5.

4.2. Biased transmission spectra

We used ExoTETHyS.BOATS to calculate the bias in transit depth on the same wavelength bins as the transmission spectra. Table 2 reports the system parameters. Table 3 contains the dayside and nightside temperatures based on current estimates from observations. We modeled the emission from the two planetary hemispheres in the following ways:

- assuming blackbody spectra with T_{day} and T_{night} from Table 3 (most likely configurations) and
- calculating the emission spectra with Tau-REx III, assuming ACE with solar C/O ratio (and C/O=1.5) and metallicity, CIA, Rayleigh scattering, and temperature profiles as in Guillot (2010) with the same T_{day} and T_{night} .

We then added the spectroscopic bias in three forms to the pure transmission spectra to obtain the biased spectra:

- total bias resulting from the self- and phase-blend effects;
- total bias minus average offset, such that the sum of the biases on the wavelength bins is zero; and
- self-blend bias only.

The case of total bias minus average offset may occur if a constant correction is applied at all wavelengths. For example, when the spectral light curves are divided by the white one (e.g., Tsiaras et al. 2016), if the bias in transit depth is removed for white light curve, the spectral values will also be shifted, but they remain biased. The self-blend bias is what remains if the phase-blend effect is removed from the data for each wavelength (Martin-Lagarde et al. 2020). Figure 4 shows the pure transmission and biased spectra considered for WASP 12 b and WASP 43 b. The biased spectra appear to have an

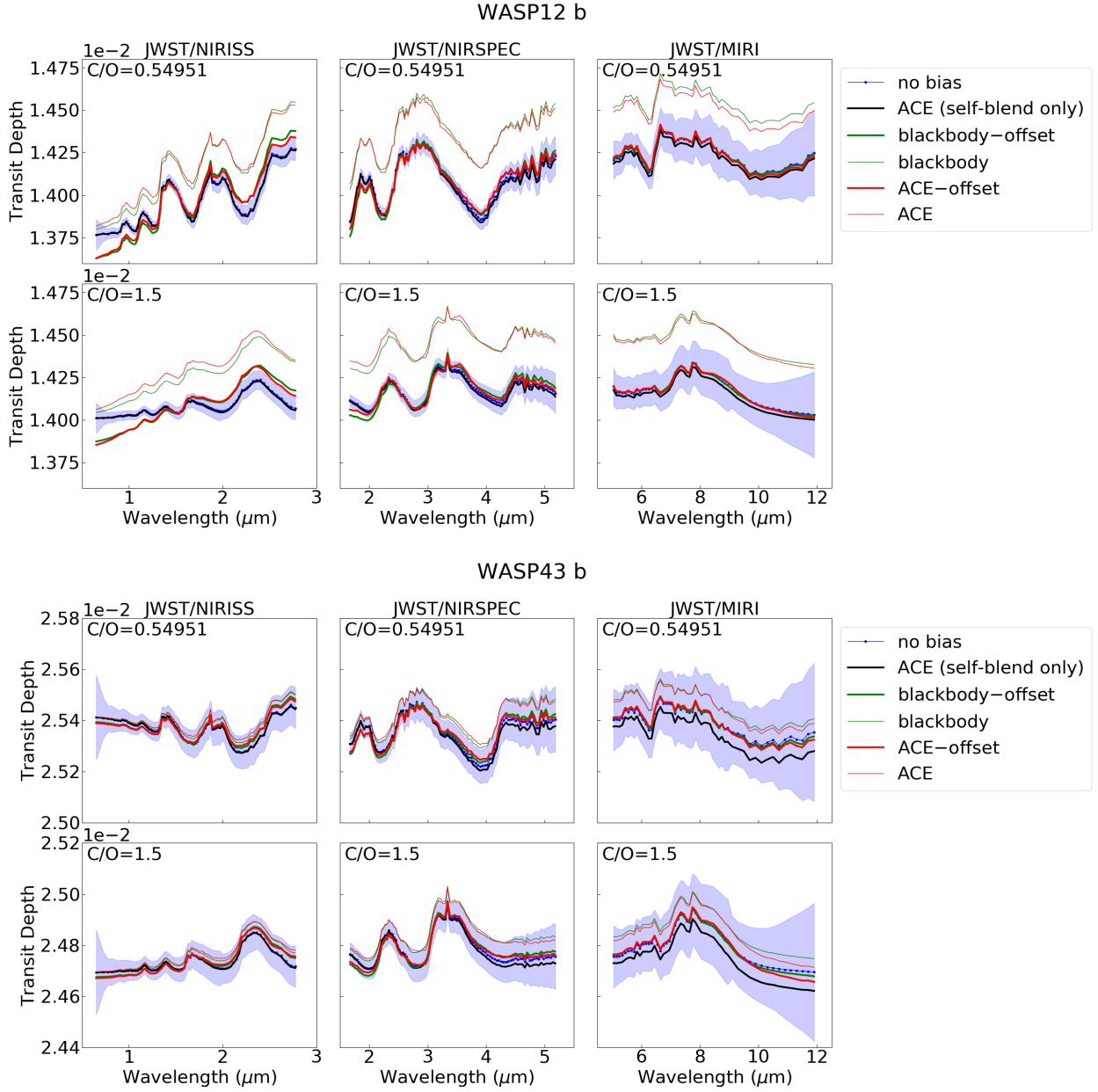


Figure 4. Simulated transmission spectra for WASP 12 b and WASP 43 b. Each panel contains a set of spectra for a specific JWST instrument (from left to right: NIRISS, NIRSpec, and MIRI) and atmospheric C/O ratio (upper rows: solar C/O; lower rows: C/O=1.5). The pure transmission spectra (no bias added) are in blue, with a swath denoting the 1σ error bars estimated by using ExoTETHyS.BOATS. The other spectra are biased as described in Section 4.2. The “model–offset” assumes a constant correction that does not account for the wavelength dependence of the bias. A significantly biased spectral slope is observed for WASP 12 b with NIRISS ($\gg 1\sigma$), and in the bluer part of the NIRSPEC spectra $\gtrsim 1\sigma$, and there is a large but nearly constant offset with MIRI. The biased spectra for WASP 43 b are almost entirely within the 1σ error bars.

offset and a different slope than the pure transmission ones in the NIRISS passband. The effect on the slope is smaller at the longer wavelengths, and it is negligible in the MIRI passband. The bias for WASP 12 b is much larger than the 1σ error bars in most configurations, while for WASP 43 b it is within about 1σ .

4.3. Atmospheric retrievals

We performed atmospheric retrievals on the pure and biased transmission spectra using Tau-REx III. The free fitting parameters were the planet radius, the isothermal temperature, three Mie scattering parameters, and the abundances of all of the molecules used by the ACE module to compute the transmission spectra. We take

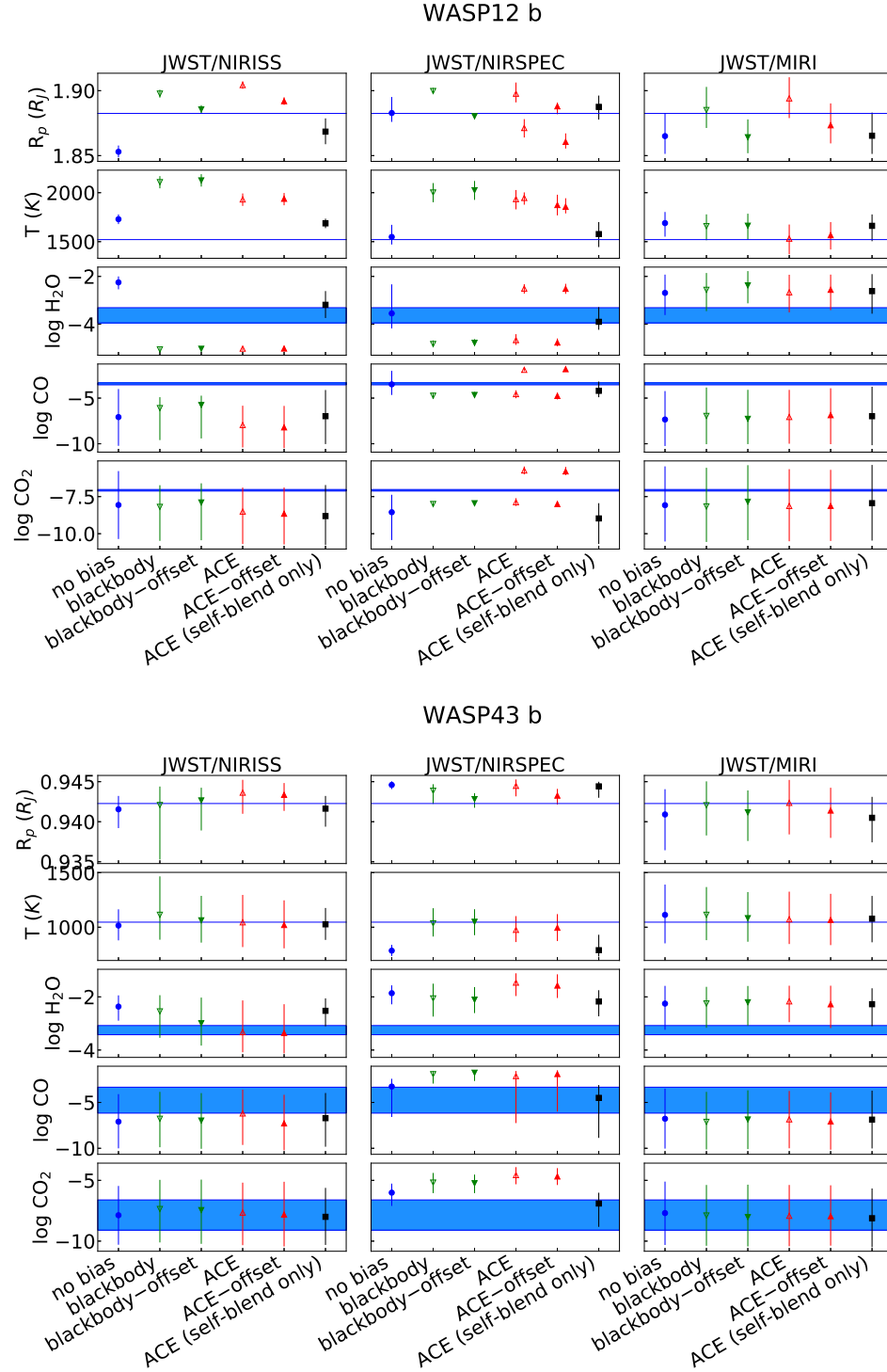


Figure 5. Parameters retrieved from the simulated transmission spectra for WASP 12 b and WASP 43 b shown in Figure 4 (cases with with solar C/O ratio). For the NIRSpec spectra of WASP 12 b with ACE and ACE–offset bias, the retrieval algorithm found two statistically equivalent solutions, which are both reported. The blue horizontal lines indicate the input parameter values, and the shaded areas indicate the range of molecular mixing ratios at various heights in the atmosphere (the mixing ratios are kept constant in the retrievals). Where the spectral slope was largely biased, the retrieved atmospheric temperature and water mixing ratio can be significantly different from those obtained from the unbiased spectra (WASP 12 b; NIRISS and NIRSpec). A constant offset appears to only affect the inferred planet’s radius (WASP 12 b; MIRI). In a few cases, the parameters retrieved from the unbiased spectra do not match the input values, likely due to approximations adopted in the retrievals or degeneracies.

the approximation of uniform chemical distribution with height for the retrievals, neglecting the pressure dependence of the input models.

4.4. Biases in retrieval results

In all cases, the retrieval algorithm found a solution that provides an excellent match to the simulated spectrum, albeit with different than input parameters. Figure 5 compares the atmospheric parameters retrieved from pure and biased transmission spectra with their underlying values and/or intervals from the input models. The spectrum bias can affect the H₂O abundance measured on WASP 12 b by orders of magnitude, the temperature by ~ 500 K, and the planet radius by 2-3%. In some cases, the measured discrepancies may include the effect of parameter degeneracies, which are discussed below. The largest effects occur with JWST/NIRISS, for which the biased spectra have a significantly different slope than the pure transmission ones. We obtained similar trends using blackbody or ACE spectra for planetary emission, but it is possible to have larger differences in the presence of more pronounced molecular features. The constant offsets change only the apparent radius of the planet, but not the other atmospheric parameters.

Unsurprisingly, the parameters obtained for WASP 43 b are not significantly affected by the modest spectroscopic bias. If the phase-blend effect is corrected, the self-blend bias is negligible for both WASP 12 b and WASP 43 b.

We note that, in some cases, the retrieved parameters do not match the underlying values even in the absence of spectrum bias. These discrepancies can only be partially explained by the approximation of constant gas profiles adopted in the retrievals (Changeat et al. 2019). The error bars obtained from atmospheric retrievals can sometimes be underestimated, not accounting for the full parameter degeneracies (Rocchetto et al. 2016). Performing retrievals over the broader wavelength range covered by the three instruments should help to significantly reduce the degeneracies between the planet’s radius and atmospheric parameters (Chapman et al. 2017; Welbanks & Madhusudhan 2019). A discussion of the robustness of the retrievals themselves is beyond the scope of this paper.

5. PREDICTED IMPACT ON FUTURE OBSERVATIONS

We calculated the bias spectra for all exoplanets that will be observed in the JWST GTO and ERS programs as described in Section 4.2 with blackbody emission spectra. Table 2 reports the system parameters. Table 3 reports the dayside and nightside temperatures

based on current estimates from observations and their theoretical limits. Tables 4 and 5 show the mean offsets and peak-to-peak amplitudes of the spectroscopic bias for the different configurations. For most planets, the spectroscopic bias is smaller than the 1σ error bars. The only JWST GTO and ERS targets showing a potential bias larger than 3σ with a single visit are WASP 121 b, WASP 18 b, WASP 77A b, WASP 43 b, and HD189733 b (see Table 5). It is worth noting that phase-blend is the dominant bias component for four out of five planets, which can be largely removed by appropriate data detrending. Furthermore, the full phase curves of WASP121 b and WASP 43 b will be observed. The only target with a potentially significant self-blend bias is HD189733 b, but it should not affect the secondary eclipse observations that are currently scheduled.

Figures 6 and 7 provide color maps to highlight regions of the parameter space from which the exoplanet spectra observed with JWST are more likely to be affected by the self- and phase-blend effects. In general, we can have spectral biases larger than 10 ppm for Neptune-sized or larger planets. The phase-blend bias can be up to hundreds of ppm for hot Jupiters with periods shorter than 2 days. The self-blend bias is more weakly dependent on the orbital period, but it rarely exceeds the 100 ppm.

Future transmission spectra taken with the Ariel mission can also be affected by the dark planet approximation. The general trends inferred for the JWST spectra can be extended to the Ariel ones, with some quantitative differences due to the specific instruments. Ariel will simultaneously cover the spectral region 0.5-7.8 μm , thus comprising the wavelength range of JWST/NIRSpec, and partly also that of NIRISS and MIRI. The Ariel spectra will have lower resolution, especially at wavelengths shorter than 2 μm . Due to the different telescope apertures, the Ariel mission will require multiple visits to achieve the same signal-to-noise ratio that would be obtained with a single JWST visit.

6. CONCLUSIONS

In this paper, we studied the impact of the common dark planet approximation in transit spectroscopy. We adopted the novel ExoTETHyS.BOATS subpackage to calculate the transit depth bias on simulated spectra with the JWST. This newly released software relies on the formulae derived by Martin-Lagarde et al. (2020) (the core algorithm was already used in that study). We find that, in some cases, these biases can significantly affect the parameters obtained from atmospheric retrievals, including gas temperature and mixing ratios. These effects are more important for large-radius,

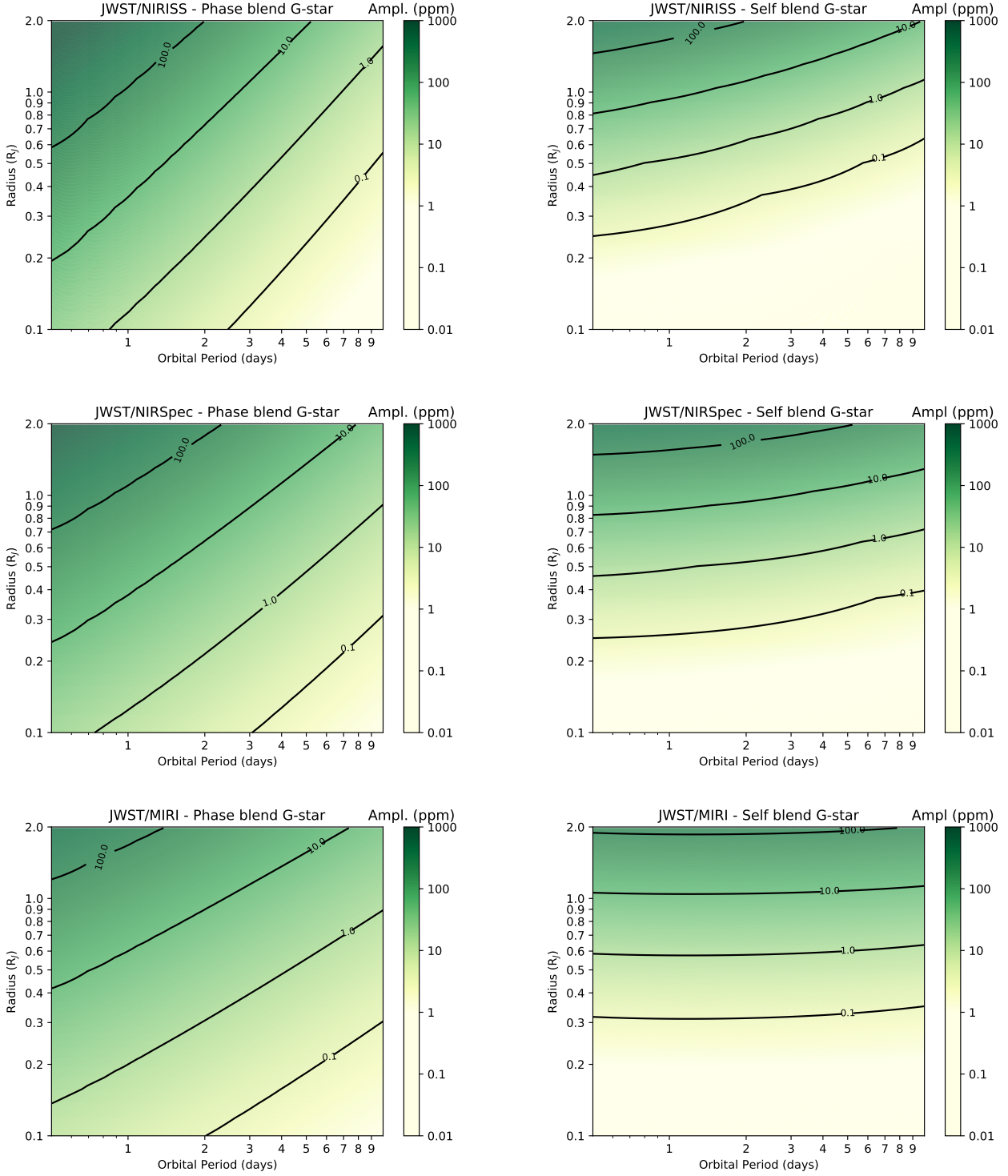


Figure 6. Color maps with orbital period vs. planet’s radius showing the peak-to-peak amplitude of the spectral biases for the JWST transmission spectra of exoplanets around a star with $T_{*,\text{eff}} = 5800\text{ K}$, solar mass and radius. We consider transits with impact parameter $b = 0.5$, for homogeneity. The left column reports the results for the phase-blend bias (with $\varepsilon = 0.0$), and the right column reports those for the self-blend bias (with $\varepsilon = 1.0$).

short-period planets. The color dependence appears to be stronger in near-infrared spectra and/or when combining UV/visible with mid-infrared spectra. Our re-

pective reanalysis for observations already planned within the JWST GTO and ERS programs did not reveal any critical issues, either because the bias is negli-

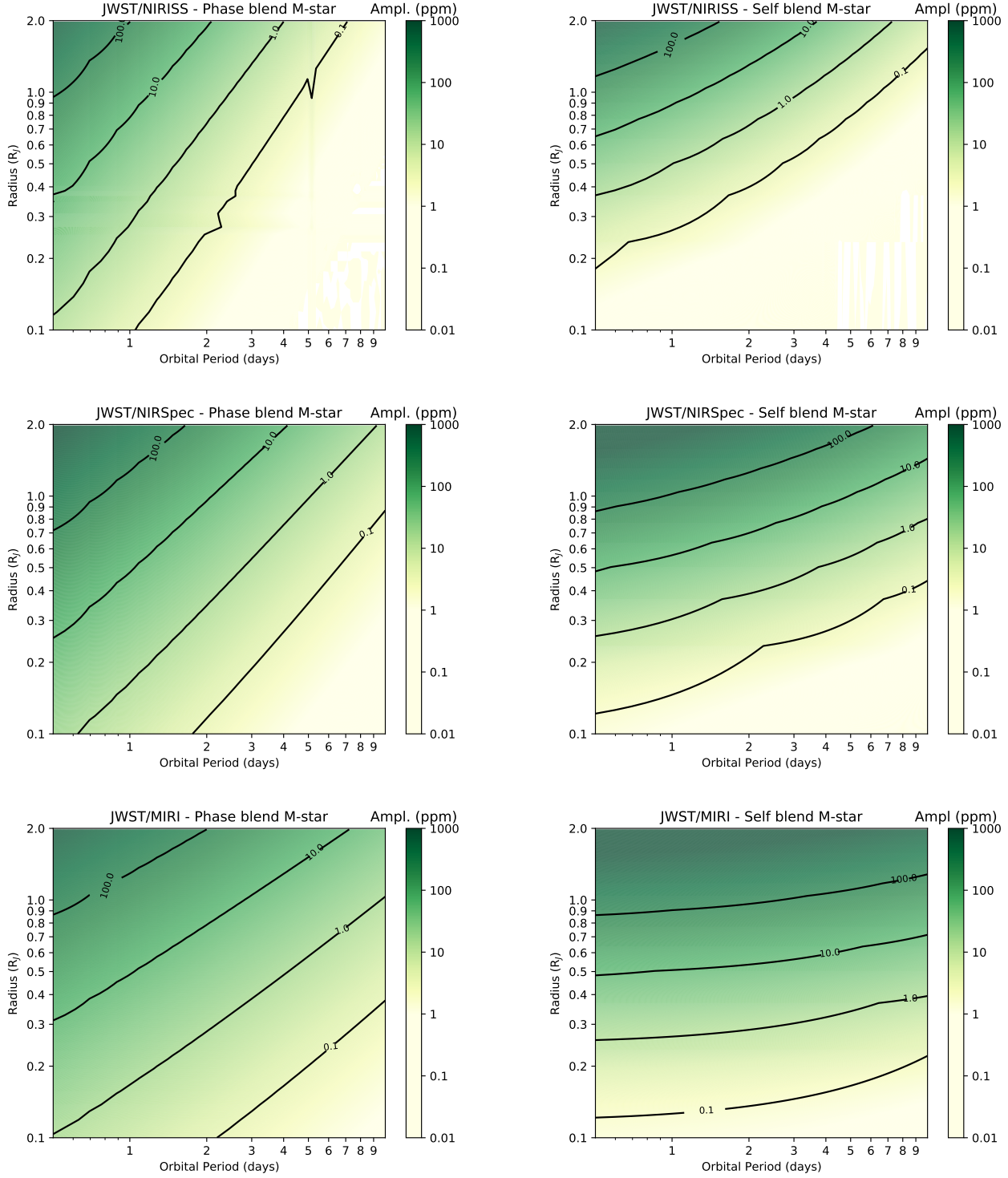


Figure 7. Color maps analogous to those in Figure 6, but for an M dwarf with $T_{*,\text{eff}} = 3800\text{ K}$, $M = 0.51 M_{\odot}$, and $R = 0.60 R_{\odot}$. The contour lines in the upper left panel appear to be unsmooth because of numerical precision at the <1 ppm level.

gible or it should be detrendable from the data. We also provide precalculated tables and color maps as quick-look tools to assess the potential impact of self- and phase-blend biases on specific targets. Knowing in ad-

vance an estimate of the bias can guide the selection of targets and/or the choice of the type of observation.

ACKNOWLEDGMENTS

We thank the anonymous referee for their helpful suggestions. G.M. thanks Q. Changeat, C. Cossou, D. Dicken, and I. P. Waldmann for useful discussions. This work was supported by the LabEx P2IO, the French ANR contract 05-BLANNT09-573739, and the European Union's Horizon 2020 Research and Innovation Programme (grant agreement No. 776403). T.Z. has been funded by the European Research Council (ERC) under the European Union's Horizon 2020 Research and Innovation Programme (grant agreement No. 679030/WHIPLASH).

Table 4. Transit depth biases and error bars estimated for the most likely configurations (see Table 3). The offset is the mean value of the bias over the wavelength bins. The amplitude is the difference between the maximum and minimum bias over the wavelength bins. Numbers in bold denote bias values greater than three times the nominal error bar, and greater than 30 ppm. (This table is available in machine-readable form.)

Planet	Instrument	Total bias		Self-blend bias		Error bar
		Offset	Amplitude	Offset	Amplitude	
WASP 12 b	NIRISS	+170	242	-4	9	42
	NIRSpec	+275	119	-12	17	57
	MIRI	+303	13	-27	13	131
WASP 43 b	NIRISS	+20	52	-1	5	55
	NIRSpec	+58	58	-10	25	65
	MIRI	+69	25	-46	44	143
WASP 121 b	NIRISS	+157	241	-4	9	29
	NIRSpec	+266	127	-13	19	40
	MIRI	+298	14	-32	18	93
WASP 18 b	NIRISS	+85	138	-9e-1	1	19
	NIRSpec	+159	108	-2	1	26
	MIRI	+217	28	-3	2	60
WASP 79 b	NIRISS	+2	3	-1	5	23
	NIRSpec	+1	5	-6	11	31
	MIRI	-6	7	-16	8	73
WASP 80 b	NIRISS	-2e-1	2	-4e-1	3	26
	NIRSpec	-7	22	-8	25	30
	MIRI	-48	58	-53	60	64
WASP 17 b	NIRISS	-6	18	-6	18	33
	NIRSpec	-22	32	-22	32	46
	MIRI	-47	20	-47	20	106
WASP 39 b	NIRISS	-1	7	-1	7	47
	NIRSpec	-12	26	-12	26	60
	MIRI	-42	31	-42	31	137
WASP 69 b	NIRISS	-4e-1	3	-4e-1	3	16
	NIRSpec	-5	14	-5	14	19
	MIRI	-25	22	-25	22	43
HD 189733 b	NIRISS	+2e-1	2	-1	6	7
	NIRSpec	-6	19	-11	27	9
	MIRI	-36	37	-46	39	19
HD 209458 b	NIRISS	+2	4	-3e-1	1	7
	NIRSpec	+4	3	-3	8	9
	MIRI	-2	9	-13	12	21

Table 4 continued

Table 4 (*continued*)

Planet	Instrument	Total bias		Self-blend bias		Error bar
		Offset	Amplitude	Offset	Amplitude	
HD 149026 b	NIRISS	+1	3	-1e-2	6e-2	9
	NIRSpec	+3	3	-1e-1	2e-1	12
	MIRI	+5	4e-1	-4e-1	3e-1	27
HAT-P-1 b	NIRISS	+2e-1	6e-1	-4e-1	2	25
	NIRSpec	-2	6	-4	8	33
	MIRI	-10	9	-14	10	76
HAT-P-26 b	NIRISS	+3e-2	3e-2	-4e-3	3e-2	39
	NIRSpec	-9e-2	4e-1	-1e-1	4e-1	49
	MIRI	-1	1	-1	1	110
GJ 436 b	NIRISS	+1e-2	6e-2	-4e-4	4e-3	13
	NIRSpec	+1e-1	3e-1	-4e-2	2e-1	13
	MIRI	-4e-2	1	-8e-1	2	27
GJ 3470 b	NIRISS	+2e-2	4e-3	-4e-4	4e-3	24
	NIRSpec	-1e-2	1e-1	-3e-2	1e-1	26
	MIRI	-6e-1	1	-6e-1	1	54

Table 5. Transit depth biases and error bars estimated for the extreme configurations (see Table 3). (This table is available in machine-readable form.)

Planet	Instrument	Total bias		Self-blend bias		Error bar
		Offset	Amplitude	Offset	Amplitude	
WASP 12 b	NIRISS	+257 /-19	354 /36	-4/-19	6/36	42
	NIRSpec	+423 /-41	229 /34	-7/-41	4/34	57
	MIRI	+549 /-61	75/13	-9/-61	1/13	131
WASP 43 b	NIRISS	+30/-10	80/34	-9e-1/-10	2/34	55
	NIRSpec	+95/-47	118 /79	-3/-47	3/79	65
	MIRI	+179/-117	61/59	-5/-117	2/59	143
WASP 121 b	NIRISS	+171 /-21	271 /45	-3/-21	5/45	29
	NIRSpec	+312 /-51	203 /49	-6/-51	4/49	40
	MIRI	+428 /-82	71/21	-8/-82	1/21	93
WASP 18 b	NIRISS	+98 /-7	152 /14	-1/-7	2/14	19
	NIRSpec	+175 /-16	110 /15	-2/-16	1/15	26
	MIRI	+238 /-26	38/6	-3/-26	4e-1/6	60
WASP 79 b	NIRISS	+7/-2	17/7	-9e-2/-2	2e-1/7	23
	NIRSpec	+19/-9	21/13	-2e-1/-9	3e-1/13	31
	MIRI	+34/-19	10/8	-4e-1/-19	1e-1/8	73
WASP 80 b	NIRISS	+7e-1/-6e-1	3/4	-2e-2/-6e-1	1e-1/4	26
	NIRSpec	+6/-11	13/32	-2e-1/-11	5e-1/32	30
	MIRI	+21/-62	16/65	-7e-1/-62	6e-1/65	64

Table 5 *continued*

Table 5 (*continued*)

Planet	Instrument	Total bias		Self-blend bias		Error bar
		Offset	Amplitude	Offset	Amplitude	
WASP 17 b	NIRISS	+16/-6	36/19	-3e-1/-6	7e-1/19	33
	NIRSpec	+41/-24	43/33	-8e-1/-24	8e-1/33	46
	MIRI	+69/-49	19/20	-1/-49	4e-1/20	106
WASP 39 b	NIRISS	+1/-1	5/7	-4e-2/-1	1e-1/7	47
	NIRSpec	+7/-12	13/27	-2e-1/-12	3e-1/27	60
	MIRI	+19/-43	10/31	-5e-1/-43	2e-1/31	137
WASP 69 b	NIRISS	+5e-1/-5e-1	2/3	-1e-2/-5e-1	4e-2/3	16
	NIRSpec	+3/-6	6/15	-7e-2/-6	1e-1/15	19
	MIRI	+10/-26	6/23	-2e-1/-26	1e-1/23	43
HD 189733 b	NIRISS	+4/-3	12/14	-1e-1/-3	3e-1/14	7
	NIRSpec	+16/-22	24/ 44	-4e-1/-22	7e-1/ 44	9
	MIRI	+36/ -68	16/44	-1/ -68	4e-1/44	19
HD 209458 b	NIRISS	+4/-2	12/8	-7e-2/-2	2e-1/8	7
	NIRSpec	+14/-11	19/20	-2e-1/-11	3e-1/20	9
	MIRI	+28/-29	10/15	-5e-1/-29	2e-1/15	21
HD 149026 b	NIRISS	+2/-1e-1	5/4e-1	-6e-3/-1e-1	1e-2/4e-1	9
	NIRSpec	+6/-5e-1	7/7e-1	-2e-2/-5e-1	2e-2/7e-1	12
	MIRI	+11/-1	3/4e-1	-3e-2/-1	8e-3/4e-1	27

Table 5 *continued*

Table 5 (*continued*)

Planet	Instrument	Total bias		Self-blend bias		Error bar
		Offset	Amplitude	Offset	Amplitude	
HAT-P-1 b	NIRISS	+1/-1	4/4	-2e-2/-1	6e-2/4	25
	NIRSpec	5/-6	7/12	-7e-2/-6	1e-1/12	33
	MIRI	+11/-18	5/11	-2e-1/-18	7e-2/11	76
HAT-P-26 b	NIRISS	+2e-1/-6e-2	1/3e-1	-2e-3/-6e-2	6e-3/3e-1	39
	NIRSpec	+1/-6e-1	3/2	-9e-3/-6e-1	2e-2/2	49
	MIRI	+4/-3	2/2	-2e-2/-3	1e-2/2	110
GJ 436 b	NIRISS	+1e-2/-7e-3	9e-2/6e-2	-1e-4/-7e-3	7e-4/6e-2	13
	NIRSpec	+2e-1/-3e-1	6e-1/9e-1	-2e-3/-3e-1	5e-3/9e-1	13
	MIRI	+1/-2	1/3	-9e-3/-2	9e-3/3	27
GJ 3470 b	NIRISS	+3e-2/-6e-3	2e-1/5e-2	-2e-4/-6e-3	1e-3/5e-2	24
	NIRSpec	+4e-1/-2e-1	1/6e-1	-3e-3/-2e-1	7e-3/6e-1	26
	MIRI	+2/-1	2/2	-1e-2/-1	1e-2/2	54
WASP 77A b	NIRISS	+35/-7	79/21	-7e-1/-7	2/21	24
	NIRSpec	+90/-26	94/38	-2/-26	2/38	31
	MIRI	+152/-56	42/23	-3/-56	8e-1/23	71
WASP 52 b	NIRISS	+10/-6	30/26	-3e-1/-6	9e-1/26	58
	NIRSpec	+36/-37	51/69	-1/-37	2/69	73
	MIRI	+76/-104	31/60	-2/-104	1/60	164
WASP 127 b	NIRISS	+4/-1	12/5	-6e-2/-1	2e-1/5	18
	NIRSpec	+14/-7	19/13	-2e-1/-7	3e-1/13	24
	MIRI	+29/-19	11/10	-4e-1/-19	1e-1/10	55
WASP 107 b	NIRISS	+1e-1/-1e-1	6e-1/9e-1	-2e-3/-1e-1	1e-2/9e-1	24
	NIRSpec	+1/-3	3/10	-3e-2/-3	7e-2/10	29
	MIRI	+5/-21	5/26	-1e-1/-21	1e-1/26	63
TOI 193 b	NIRISS	+4/-2e-1	7/6e-1	-9e-3/-2e-1	2e-2/6e-1	30
	NIRSpec	+8/-7e-1	6/8e-1	-2e-2/-7e-1	1e-2/8e-1	39
	MIRI	+11/-1	2/4e-1	-3e-2/-1	6e-3/4e-1	88
GJ 1214 b	NIRISS	+3e-2/-1e-2	2e-1/1e-1	-5e-4/-1e-2	3e-3/1e-1	53
	NIRSpec	+6e-1/-6e-1	2/2	-1e-2/-6e-1	3e-2/2	49
	MIRI	+4/-8	5/12	-7e-2/-8	8e-2/12	99
GJ 357 b	NIRISS	+3e-4/-2e-5	2e-3/2e-4	-3e-7/-2e-5	3e-6/2e-4	14
	NIRSpec	+9e-3/-2e-3	3e-2/7e-3	-1e-5/-2e-3	4e-5/7e-3	15
	MIRI	+7e-2/-3e-2	1e-1/5e-2	-9e-5/-3e-2	1e-4/5e-2	31
GJ 1132 b	NIRISS	+3e-3/-3e-4	3e-2/3e-3	-1e-5/-3e-4	7e-5/3e-3	45
	NIRSpec	+7e-2/-2e-2	2e-1/8e-2	-2e-4/-2e-2	7e-4/8e-2	45
	MIRI	+5e-1/-2e-1	6e-1/4e-1	-1e-3/-2e-1	2e-3/4e-1	92
L98-59 c	NIRISS	+3e-4/-3e-5	3e-3/3e-4	-5e-7/-3e-5	5e-6/3e-4	19
	NIRSpec	+1e-2/-3e-3	4e-2/1e-2	-2e-5/-3e-3	7e-5/1e-2	19
	MIRI	+1e-1/-5e-2	1e-1/9e-2	-2e-4/-5e-2	2e-4/9e-2	39

Table 5 *continued*

Table 5 (*continued*)

Planet	Instrument	Total bias		Self-blend bias		Error bar
		Offset	Amplitude	Offset	Amplitude	
L98-59 d	NIRISS	+3e-6/-2e-6	4e-5/4e-5	-7e-9/-2e-6	8e-8/4e-5	24
	NIRSpec	+3e-4/-1e-3	1e-3/5e-3	-8e-7/-1e-3	3e-6/5e-3	25
	MIRI	+5e-3/-4e-2	1e-2/9e-2	-1e-5/-4e-2	2e-5/9e-2	51
LP 791-18 b	NIRISS	+1e-2/-1e-3	8e-2/1e-2	-4e-5/-1e-3	3e-4/1e-2	163
	NIRSpec	+2e-1/-5e-2	6e-1/2e-1	-8e-4/-5e-2	2e-3/2e-1	150
	MIRI	+1/-6e-1	1/8e-1	-5e-3/-6e-1	5e-3/8e-1	299
Trappist-1 b	NIRISS	+3e-4/-5e-5	4e-3/8e-4	-3e-6/-5e-5	3e-5/8e-4	138
	NIRSpec	+3e-2/-2e-2	1e-1/1e-1	-2e-4/-2e-2	1e-3/1e-1	107
	MIRI	+4e-1/-6e-1	8e-1/2	-4e-3/-6e-1	6e-3/2	202
Trappist-1 d	NIRISS	+5e-7/-6e-8	9e-6/1e-6	-2e-9/-6e-8	4e-8/1e-6	119
	NIRSpec	+3e-4/-2e-4	2e-3/2e-3	-1e-6/-2e-4	8e-6/2e-3	92
	MIRI	+2e-2/-3e-2	4e-2/1e-1	-6e-5/-3e-2	2e-4/1e-1	174
Trappist-1 e	NIRISS	+5e-8/-6e-9	9e-7/2e-7	-2e-10/-6e-9	5e-9/2e-7	111
	NIRSpec	+7e-5/-9e-5	5e-4/7e-4	-4e-7/-9e-5	3e-6/7e-4	86
	MIRI	+6e-3/-3e-2	2e-2/1e-1	-4e-5/-3e-2	1e-4/1e-1	163
Trappist-1 f	NIRISS	+2e-9/-4e-10	5e-8/1e-8	-2e-11/-4e-10	4e-10/1e-8	105
	NIRSpec	+1e-5/-2e-5	9e-5/2e-4	-9e-8/-2e-5	7e-7/2e-4	82
	MIRI	+2e-3/-2e-2	8e-3/1e-1	-2e-5/-2e-2	6e-5/1e-1	154

REFERENCES

- Agúndez, M., Venot, O., Iro, N., et al. 2012, *A&A*, 548, A73, doi: [10.1051/0004-6361/201220365](https://doi.org/10.1051/0004-6361/201220365)
- Al-Refaie, A. F., Changeat, Q., Waldmann, I. P., & Tinetti, G. 2019, arXiv e-prints, arXiv:1912.07759. <https://arxiv.org/abs/1912.07759>
- Anderson, D. R., Smith, A. M. S., Lanotte, A. A., et al. 2011, *MNRAS*, 416, 2108, doi: [10.1111/j.1365-2966.2011.19182.x](https://doi.org/10.1111/j.1365-2966.2011.19182.x)
- Anderson, D. R., Collier Cameron, A., Delrez, L., et al. 2017, *A&A*, 604, A110, doi: [10.1051/0004-6361/201730439](https://doi.org/10.1051/0004-6361/201730439)
- Arcangeli, J., Désert, J.-M., Parmentier, V., et al. 2019, *A&A*, 625, A136, doi: [10.1051/0004-6361/201834891](https://doi.org/10.1051/0004-6361/201834891)
- Auvergne, M., Bodin, P., Boisnard, L., et al. 2009, *A&A*, 506, 411, doi: [10.1051/0004-6361/200810860](https://doi.org/10.1051/0004-6361/200810860)
- Bakos, G., Noyes, R. W., Kovács, G., et al. 2004, *PASP*, 116, 266, doi: [10.1086/382735](https://doi.org/10.1086/382735)
- Bakos, G. Á., Csubry, Z., Penev, K., et al. 2013, *PASP*, 125, 154, doi: [10.1086/669529](https://doi.org/10.1086/669529)
- Barstow, J. K., Aigrain, S., Irwin, P. G. J., & Sing, D. K. 2017, *ApJ*, 834, 50, doi: [10.3847/1538-4357/834/1/50](https://doi.org/10.3847/1538-4357/834/1/50)
- Bean, J. L., Stevenson, K. B., Batalha, N. M., et al. 2018, *PASP*, 130, 114402, doi: [10.1088/1538-3873/aadbf3](https://doi.org/10.1088/1538-3873/aadbf3)
- Beaulieu, J. P., Tinetti, G., Kipping, D. M., et al. 2011, *ApJ*, 731, 16, doi: [10.1088/0004-637X/731/1/16](https://doi.org/10.1088/0004-637X/731/1/16)
- Beichman, C., Benneke, B., Knutson, H., et al. 2014, *PASP*, 126, 1134, doi: [10.1086/679566](https://doi.org/10.1086/679566)
- Bell, T. J., Zhang, M., Cubillos, P. E., et al. 2019, *MNRAS*, 489, 1995, doi: [10.1093/mnras/stz2018](https://doi.org/10.1093/mnras/stz2018)
- Benneke, B., Wong, I., Piaulet, C., et al. 2019a, *ApJL*, 887, L14, doi: [10.3847/2041-8213/ab59dc](https://doi.org/10.3847/2041-8213/ab59dc)
- Benneke, B., Knutson, H. A., Lothringer, J., et al. 2019b, *Nature Astronomy*, 3, 813, doi: [10.1038/s41550-019-0800-5](https://doi.org/10.1038/s41550-019-0800-5)
- Berta-Thompson, Z. K., Irwin, J., Charbonneau, D., et al. 2015, *Nature*, 527, 204, doi: [10.1038/nature15762](https://doi.org/10.1038/nature15762)
- Biddle, L. I., Pearson, K. A., Crossfield, I. J. M., et al. 2014, *MNRAS*, 443, 1810, doi: [10.1093/mnras/stu1199](https://doi.org/10.1093/mnras/stu1199)
- Bonomo, A. S., Desidera, S., Benatti, S., et al. 2017, *A&A*, 602, A107, doi: [10.1051/0004-6361/201629882](https://doi.org/10.1051/0004-6361/201629882)
- Borucki, W. J., Koch, D., Basri, G., et al. 2010, *Science*, 327, 977, doi: [10.1126/science.1185402](https://doi.org/10.1126/science.1185402)

- Brown, D. J. A., Triaud, A. H. M. J., Doyle, A. P., et al. 2017, *MNRAS*, 464, 810, doi: [10.1093/mnras/stw2316](https://doi.org/10.1093/mnras/stw2316)
- Changeat, Q., Edwards, B., Waldmann, I. P., & Tinetti, G. 2019, *ApJ*, 886, 39, doi: [10.3847/1538-4357/ab4a14](https://doi.org/10.3847/1538-4357/ab4a14)
- Chapman, J. W., Zellem, R. T., Line, M. R., et al. 2017, *PASP*, 129, 104402, doi: [10.1088/1538-3873/aa84a9](https://doi.org/10.1088/1538-3873/aa84a9)
- Charbonneau, D., Brown, T. M., Noyes, R. W., & Gilliland, R. L. 2002, *ApJ*, 568, 377, doi: [10.1086/338770](https://doi.org/10.1086/338770)
- Chen, G., Pallé, E., Nortmann, L., et al. 2017, *A&A*, 600, L11, doi: [10.1051/0004-6361/201730736](https://doi.org/10.1051/0004-6361/201730736)
- Chen, G., Pallé, E., Welbanks, L., et al. 2018, *A&A*, 616, A145, doi: [10.1051/0004-6361/201833033](https://doi.org/10.1051/0004-6361/201833033)
- Chubb, K. L., Min, M., Kawashima, Y., Helling, C., & Waldmann, I. 2020, *A&A*, 639, A3, doi: [10.1051/0004-6361/201937267](https://doi.org/10.1051/0004-6361/201937267)
- Chubb, K. L., Rocchetto, M., Yurchenko, S. N., et al. 2021, *A&A*, 646, A21, doi: [10.1051/0004-6361/202038350](https://doi.org/10.1051/0004-6361/202038350)
- Collins, K. A., Kielkopf, J. F., & Stassun, K. G. 2017, *AJ*, 153, 78, doi: [10.3847/1538-3881/153/2/78](https://doi.org/10.3847/1538-3881/153/2/78)
- Cowan, N. B., & Agol, E. 2011, *ApJ*, 729, 54, doi: [10.1088/0004-637X/729/1/54](https://doi.org/10.1088/0004-637X/729/1/54)
- Cowan, N. B., Machalek, P., Croll, B., et al. 2012, *ApJ*, 747, 82, doi: [10.1088/0004-637X/747/1/82](https://doi.org/10.1088/0004-637X/747/1/82)
- Crossfield, I. J. M., Waalkes, W., Newton, E. R., et al. 2019, *ApJL*, 883, L16, doi: [10.3847/2041-8213/ab3d30](https://doi.org/10.3847/2041-8213/ab3d30)
- Damiano, M., Morello, G., Tsiaras, A., Zingales, T., & Tinetti, G. 2017, *AJ*, 154, 39, doi: [10.3847/1538-3881/aa738b](https://doi.org/10.3847/1538-3881/aa738b)
- Danielski, C., Deroo, P., Waldmann, I. P., et al. 2014, *ApJ*, 785, 35, doi: [10.1088/0004-637X/785/1/35](https://doi.org/10.1088/0004-637X/785/1/35)
- Daylan, T., Günther, M. N., Mikal-Evans, T., et al. 2021, *AJ*, 161, 131, doi: [10.3847/1538-3881/abd8d2](https://doi.org/10.3847/1538-3881/abd8d2)
- Delrez, L., Santerne, A., Almenara, J. M., et al. 2016, *MNRAS*, 458, 4025, doi: [10.1093/mnras/stw522](https://doi.org/10.1093/mnras/stw522)
- Deming, D., Wilkins, A., McCullough, P., et al. 2013, *ApJ*, 774, 95, doi: [10.1088/0004-637X/774/2/95](https://doi.org/10.1088/0004-637X/774/2/95)
- Ducrot, E., Gillon, M., Delrez, L., et al. 2020, *A&A*, 640, A112, doi: [10.1051/0004-6361/201937392](https://doi.org/10.1051/0004-6361/201937392)
- Edwards, B., Changeat, Q., Baeyens, R., et al. 2020, *AJ*, 160, 8, doi: [10.3847/1538-3881/ab9225](https://doi.org/10.3847/1538-3881/ab9225)
- Evans, T. M., Sing, D. K., Wakeford, H. R., et al. 2016, *ApJL*, 822, L4, doi: [10.3847/2041-8205/822/1/L4](https://doi.org/10.3847/2041-8205/822/1/L4)
- Faedi, F., Barros, S. C. C., Anderson, D. R., et al. 2011, *A&A*, 531, A40, doi: [10.1051/0004-6361/201116671](https://doi.org/10.1051/0004-6361/201116671)
- Fisher, C., & Heng, K. 2018, *MNRAS*, 481, 4698, doi: [10.1093/mnras/sty2550](https://doi.org/10.1093/mnras/sty2550)
- Fossati, L., Haswell, C. A., Froning, C. S., et al. 2010, *ApJL*, 714, L222, doi: [10.1088/2041-8205/714/2/L222](https://doi.org/10.1088/2041-8205/714/2/L222)
- Fu, G., Deming, D., Knutson, H., et al. 2017, *ApJL*, 847, L22, doi: [10.3847/2041-8213/aa8e40](https://doi.org/10.3847/2041-8213/aa8e40)
- Gaia Collaboration, Brown, A. G. A., Vallenari, A., et al. 2018, *A&A*, 616, A1, doi: [10.1051/0004-6361/201833051](https://doi.org/10.1051/0004-6361/201833051)
- Garhart, E., Deming, D., Mandell, A., et al. 2020, *AJ*, 159, 137, doi: [10.3847/1538-3881/ab6cff](https://doi.org/10.3847/1538-3881/ab6cff)
- Gillon, M., Jehin, E., Lederer, S. M., et al. 2016, *Nature*, 533, 221, doi: [10.1038/nature17448](https://doi.org/10.1038/nature17448)
- Gordon, I. E., Rothman, L. S., Hill, C., et al. 2017, *JQSRT*, 203, 3, doi: [10.1016/j.jqsrt.2017.06.038](https://doi.org/10.1016/j.jqsrt.2017.06.038)
- Guillot, T. 2010, *A&A*, 520, A27, doi: [10.1051/0004-6361/200913396](https://doi.org/10.1051/0004-6361/200913396)
- Harpsoe, K. B. W., Hardis, S., Hinse, T. C., et al. 2013, *A&A*, 549, A10, doi: [10.1051/0004-6361/201219996](https://doi.org/10.1051/0004-6361/201219996)
- Hébrard, G., Collier Cameron, A., Brown, D. J. A., et al. 2013, *A&A*, 549, A134, doi: [10.1051/0004-6361/201220363](https://doi.org/10.1051/0004-6361/201220363)
- Hellier, C., Anderson, D. R., Collier Cameron, A., et al. 2011, *A&A*, 535, L7, doi: [10.1051/0004-6361/201117081](https://doi.org/10.1051/0004-6361/201117081)
- Howell, S. B., Sobek, C., Haas, M., et al. 2014, *PASP*, 126, 398, doi: [10.1086/676406](https://doi.org/10.1086/676406)
- Irwin, P. G. J., Teanby, N. A., de Kok, R., et al. 2008, *JQSRT*, 109, 1136, doi: [10.1016/j.jqsrt.2007.11.006](https://doi.org/10.1016/j.jqsrt.2007.11.006)
- Iyer, A. R., Swain, M. R., Zellem, R. T., et al. 2016, *ApJ*, 823, 109, doi: [10.3847/0004-637X/823/2/109](https://doi.org/10.3847/0004-637X/823/2/109)
- Kammer, J. A., Knutson, H. A., Line, M. R., et al. 2015, *ApJ*, 810, 118, doi: [10.1088/0004-637X/810/2/118](https://doi.org/10.1088/0004-637X/810/2/118)
- Keating, D., & Cowan, N. B. 2017, *ApJL*, 849, L5, doi: [10.3847/2041-8213/aa8b6b](https://doi.org/10.3847/2041-8213/aa8b6b)
- Kendrew, S., Scheithauer, S., Bouchet, P., et al. 2015, *PASP*, 127, 623, doi: [10.1086/682255](https://doi.org/10.1086/682255)
- Kipping, D. M., & Tinetti, G. 2010, *MNRAS*, 407, 2589, doi: [10.1111/j.1365-2966.2010.17094.x](https://doi.org/10.1111/j.1365-2966.2010.17094.x)
- Knutson, H. A., Charbonneau, D., Cowan, N. B., et al. 2009, *ApJ*, 690, 822, doi: [10.1088/0004-637X/690/1/822](https://doi.org/10.1088/0004-637X/690/1/822)
- Knutson, H. A., Madhusudhan, N., Cowan, N. B., et al. 2011, *ApJ*, 735, 27, doi: [10.1088/0004-637X/735/1/27](https://doi.org/10.1088/0004-637X/735/1/27)
- Knutson, H. A., Lewis, N., Fortney, J. J., et al. 2012, *ApJ*, 754, 22, doi: [10.1088/0004-637X/754/1/22](https://doi.org/10.1088/0004-637X/754/1/22)
- Kostov, V. B., Schlieder, J. E., Barclay, T., et al. 2019, *AJ*, 158, 32, doi: [10.3847/1538-3881/ab2459](https://doi.org/10.3847/1538-3881/ab2459)
- Kreidberg, L., Line, M. R., Bean, J. L., et al. 2015, *ApJ*, 814, 66, doi: [10.1088/0004-637X/814/1/66](https://doi.org/10.1088/0004-637X/814/1/66)
- Lam, K. W. F., Faedi, F., Brown, D. J. A., et al. 2017, *A&A*, 599, A3, doi: [10.1051/0004-6361/201629403](https://doi.org/10.1051/0004-6361/201629403)
- Lee, J.-M., Heng, K., & Irwin, P. G. J. 2013, *ApJ*, 778, 97, doi: [10.1088/0004-637X/778/2/97](https://doi.org/10.1088/0004-637X/778/2/97)
- Line, M. R., Wolf, A. S., Zhang, X., et al. 2013, *ApJ*, 775, 137, doi: [10.1088/0004-637X/775/2/137](https://doi.org/10.1088/0004-637X/775/2/137)
- Linsky, J. L., Yang, H., France, K., et al. 2010, *ApJ*, 717, 1291, doi: [10.1088/0004-637X/717/2/1291](https://doi.org/10.1088/0004-637X/717/2/1291)

- Luque, R., Pallé, E., Kossakowski, D., et al. 2019, *A&A*, 628, A39, doi: [10.1051/0004-6361/201935801](https://doi.org/10.1051/0004-6361/201935801)
- Luque, R., Casasayas-Barris, N., Parviainen, H., et al. 2020, *A&A*, 642, A50, doi: [10.1051/0004-6361/202038703](https://doi.org/10.1051/0004-6361/202038703)
- Mancini, L., Southworth, J., Mollière, P., et al. 2019, *MNRAS*, 485, 5168, doi: [10.1093/mnras/stz661](https://doi.org/10.1093/mnras/stz661)
- Mandel, K., & Agol, E. 2002, *ApJL*, 580, L171, doi: [10.1086/345520](https://doi.org/10.1086/345520)
- Mansfield, M., Bean, J. L., Oklopčić, A., et al. 2018, *ApJL*, 868, L34, doi: [10.3847/2041-8213/aaf166](https://doi.org/10.3847/2041-8213/aaf166)
- Martin-Lagarde, M., Cossou, C., & Gastaud, R. 2021, *The Journal of Open Source Software*, 6, 2287, doi: [10.21105/joss.02287](https://doi.org/10.21105/joss.02287)
- Martin-Lagarde, M., Morello, G., Lagage, P.-O., Gastaud, R., & Cossou, C. 2020, *AJ*, 160, 197, doi: [10.3847/1538-3881/abac09](https://doi.org/10.3847/1538-3881/abac09)
- Maszkiewicz, M. 2017, in *Society of Photo-Optical Instrumentation Engineers (SPIE) Conference Series*, Vol. 10564, *Society of Photo-Optical Instrumentation Engineers (SPIE) Conference Series*, 105642Q, doi: [10.1117/12.2309161](https://doi.org/10.1117/12.2309161)
- Maxted, P. F. L., Anderson, D. R., Collier Cameron, A., et al. 2013, *PASP*, 125, 48, doi: [10.1086/669231](https://doi.org/10.1086/669231)
- May, E. M., & Stevenson, K. B. 2020, *AJ*, 160, 140, doi: [10.3847/1538-3881/aba833](https://doi.org/10.3847/1538-3881/aba833)
- Mendonça, J. M., Malik, M., Demory, B.-O., & Heng, K. 2018, *AJ*, 155, 150, doi: [10.3847/1538-3881/aaaebc](https://doi.org/10.3847/1538-3881/aaaebc)
- Micela, G. 2015, *Experimental Astronomy*, 40, 723, doi: [10.1007/s10686-014-9430-1](https://doi.org/10.1007/s10686-014-9430-1)
- Morello, G. 2018, *AJ*, 156, 175, doi: [10.3847/1538-3881/aadda4](https://doi.org/10.3847/1538-3881/aadda4)
- Morello, G., Claret, A., Martin-Lagarde, M., et al. 2020a, *The Journal of Open Source Software*, 5, 1834, doi: [10.21105/joss.01834](https://doi.org/10.21105/joss.01834)
- . 2020b, *AJ*, 159, 75, doi: [10.3847/1538-3881/ab63dc](https://doi.org/10.3847/1538-3881/ab63dc)
- Morello, G., Danielski, C., Dickens, D., Tremblin, P., & Lagage, P. O. 2019, *AJ*, 157, 205, doi: [10.3847/1538-3881/ab14e2](https://doi.org/10.3847/1538-3881/ab14e2)
- Morello, G., Tsiaras, A., Howarth, I. D., & Homeier, D. 2017, *AJ*, 154, 111, doi: [10.3847/1538-3881/aa8405](https://doi.org/10.3847/1538-3881/aa8405)
- Morello, G., Waldmann, I. P., Tinetti, G., et al. 2015, *ApJ*, 802, 117, doi: [10.1088/0004-637X/802/2/117](https://doi.org/10.1088/0004-637X/802/2/117)
- Parviainen, H., Pallé, E., Nortmann, L., et al. 2016, *A&A*, 585, A114, doi: [10.1051/0004-6361/201526313](https://doi.org/10.1051/0004-6361/201526313)
- Pearson, K. A. 2019, *AJ*, 158, 243, doi: [10.3847/1538-3881/ab4e1c](https://doi.org/10.3847/1538-3881/ab4e1c)
- Pinhas, A., Madhusudhan, N., Gandhi, S., & MacDonald, R. 2019, *MNRAS*, 482, 1485, doi: [10.1093/mnras/sty2544](https://doi.org/10.1093/mnras/sty2544)
- Pluriel, W., Whiteford, N., Edwards, B., et al. 2020, *AJ*, 160, 112, doi: [10.3847/1538-3881/aba000](https://doi.org/10.3847/1538-3881/aba000)
- Pollacco, D. L., Skillen, I., Collier Cameron, A., et al. 2006, *PASP*, 118, 1407, doi: [10.1086/508556](https://doi.org/10.1086/508556)
- Pontoppidan, K. M., Pickering, T. E., Laidler, V. G., et al. 2016, in *Society of Photo-Optical Instrumentation Engineers (SPIE) Conference Series*, Vol. 9910, *Observatory Operations: Strategies, Processes, and Systems VI*, 991016, doi: [10.1117/12.2231768](https://doi.org/10.1117/12.2231768)
- Rocchetto, M., Waldmann, I. P., Venot, O., Lagage, P. O., & Tinetti, G. 2016, *ApJ*, 833, 120, doi: [10.3847/1538-4357/833/1/120](https://doi.org/10.3847/1538-4357/833/1/120)
- Sarkar, S., Argyriou, I., Vandenbussche, B., Papageorgiou, A., & Pascale, E. 2018, *MNRAS*, 481, 2871, doi: [10.1093/mnras/sty2453](https://doi.org/10.1093/mnras/sty2453)
- Scandariato, G., & Micela, G. 2015, *Experimental Astronomy*, 40, 711, doi: [10.1007/s10686-014-9390-5](https://doi.org/10.1007/s10686-014-9390-5)
- Seager, S., & Mallén-Ornelas, G. 2003, *ApJ*, 585, 1038, doi: [10.1086/346105](https://doi.org/10.1086/346105)
- Sing, D. K., Fortney, J. J., Nikolov, N., et al. 2016, *Nature*, 529, 59, doi: [10.1038/nature16068](https://doi.org/10.1038/nature16068)
- Skaf, N., Bieger, M. F., Edwards, B., et al. 2020, *AJ*, 160, 109, doi: [10.3847/1538-3881/ab94a3](https://doi.org/10.3847/1538-3881/ab94a3)
- Southworth, J. 2010, *MNRAS*, 408, 1689, doi: [10.1111/j.1365-2966.2010.17231.x](https://doi.org/10.1111/j.1365-2966.2010.17231.x)
- Spake, J. J., Sing, D. K., Evans, T. M., et al. 2018, *Nature*, 557, 68, doi: [10.1038/s41586-018-0067-5](https://doi.org/10.1038/s41586-018-0067-5)
- Stevenson, K. B., Bean, J. L., Madhusudhan, N., & Harrington, J. 2014a, *ApJ*, 791, 36, doi: [10.1088/0004-637X/791/1/36](https://doi.org/10.1088/0004-637X/791/1/36)
- Stevenson, K. B., Bean, J. L., Seifahrt, A., et al. 2014b, *AJ*, 147, 161, doi: [10.1088/0004-6256/147/6/161](https://doi.org/10.1088/0004-6256/147/6/161)
- Stevenson, K. B., Harrington, J., Nymeyer, S., et al. 2010, *Nature*, 464, 1161, doi: [10.1038/nature09013](https://doi.org/10.1038/nature09013)
- Stevenson, K. B., Désert, J.-M., Line, M. R., et al. 2014c, *Science*, 346, 838, doi: [10.1126/science.1256758](https://doi.org/10.1126/science.1256758)
- Stevenson, K. B., Line, M. R., Bean, J. L., et al. 2017, *AJ*, 153, 68, doi: [10.3847/1538-3881/153/2/68](https://doi.org/10.3847/1538-3881/153/2/68)
- Tinetti, G., Drossart, P., Eccleston, P., et al. 2018, *Experimental Astronomy*, 46, 135, doi: [10.1007/s10686-018-9598-x](https://doi.org/10.1007/s10686-018-9598-x)
- Todorov, K., Deming, D., Harrington, J., et al. 2010, *ApJ*, 708, 498, doi: [10.1088/0004-637X/708/1/498](https://doi.org/10.1088/0004-637X/708/1/498)
- Torres, G., Winn, J. N., & Holman, M. J. 2008, *ApJ*, 677, 1324, doi: [10.1086/529429](https://doi.org/10.1086/529429)
- Triaud, A. H. M. J., Gillon, M., Ehrenreich, D., et al. 2015, *MNRAS*, 450, 2279, doi: [10.1093/mnras/stv706](https://doi.org/10.1093/mnras/stv706)
- Tsiaras, A., Waldmann, I. P., Rocchetto, M., et al. 2016, *ApJ*, 832, 202, doi: [10.3847/0004-637X/832/2/202](https://doi.org/10.3847/0004-637X/832/2/202)
- Tsiaras, A., Waldmann, I. P., Tinetti, G., Tennyson, J., & Yurchenko, S. N. 2019, *Nature Astronomy*, 3, 1086, doi: [10.1038/s41550-019-0878-9](https://doi.org/10.1038/s41550-019-0878-9)

- Tsiaras, A., Waldmann, I. P., Zingales, T., et al. 2018, *AJ*, 155, 156, doi: [10.3847/1538-3881/aaaf75](https://doi.org/10.3847/1538-3881/aaaf75)
- Venot, O., Hébrard, E., Agúndez, M., et al. 2012, *A&A*, 546, A43, doi: [10.1051/0004-6361/201219310](https://doi.org/10.1051/0004-6361/201219310)
- Venot, O., Parmentier, V., Blecic, J., et al. 2020, *ApJ*, 890, 176, doi: [10.3847/1538-4357/ab6a94](https://doi.org/10.3847/1538-4357/ab6a94)
- Vidal-Madjar, A., Lecavelier des Etangs, A., Désert, J. M., et al. 2003, *Nature*, 422, 143, doi: [10.1038/nature01448](https://doi.org/10.1038/nature01448)
- Vidal-Madjar, A., Désert, J. M., Lecavelier des Etangs, A., et al. 2004, *ApJL*, 604, L69, doi: [10.1086/383347](https://doi.org/10.1086/383347)
- Wakeford, H. R., Sing, D. K., Kataria, T., et al. 2017, *Science*, 356, 628, doi: [10.1126/science.aah4668](https://doi.org/10.1126/science.aah4668)
- Waldmann, I. P., Rocchetto, M., Tinetti, G., et al. 2015, *ApJ*, 813, 13, doi: [10.1088/0004-637X/813/1/13](https://doi.org/10.1088/0004-637X/813/1/13)
- Wallack, N. L., Knutson, H. A., Morley, C. V., et al. 2019, *AJ*, 158, 217, doi: [10.3847/1538-3881/ab2a05](https://doi.org/10.3847/1538-3881/ab2a05)
- Welbanks, L., & Madhusudhan, N. 2019, *AJ*, 157, 206, doi: [10.3847/1538-3881/ab14de](https://doi.org/10.3847/1538-3881/ab14de)
- Zellem, R. T., Lewis, N. K., Knutson, H. A., et al. 2014, *ApJ*, 790, 53, doi: [10.1088/0004-637X/790/1/53](https://doi.org/10.1088/0004-637X/790/1/53)
- Zhang, M., Knutson, H. A., Kataria, T., et al. 2018, *AJ*, 155, 83, doi: [10.3847/1538-3881/aaa458](https://doi.org/10.3847/1538-3881/aaa458)